

ELECTRONIC SUPPLEMENTARY MATERIAL

Lanthanide Coordination Polymers as Luminescent Thermometers: Integrating Theoretical Modelling with Experimental Analysis to Tune the Thermal Response

Airton G. Bispo-Jr,^{II} Leonardo F. Saraiva,^{II} Italo O. Mazali, Sergio A. M. Lima, Ana M. Pires,
Fernando A. Sigoli*

Table of contents

Supplementary note S1. Synthesis and characterization	1
Synthesis of the coordination polymers.....	1
Characterization	1
Supplementary note S2. Computational and theoretical details	3
Computational protocol	3
Theoretical details	3
Supplementary note S3 – Experimental structural characterization	12
Supplementary note S4 – Additional experimental photoluminescence data	14
Supplementary Note S5. Electronic structure and photophysical parameters of Ln^{III}-based compounds	19
Electronic structure.....	19
Photophysical parameters.....	20
Supplementary note S6. Intramolecular energy transfer (Ligand-to-Ln^{III})	22
Supplementary note S7 – Multiphonon relaxation	31
Supplementary note S8 – Ln^{III}-to-Ln^{III} energy transfer	34
Supplementary note S9 – Population dynamics and theoretical thermometry	39
Supplementary note S10 – Tutorial to calculate the matrix elements.....	44
Supplementary note S11 – Input data for the computational part.....	45
MWB52 ECP for Eu^{III} in Orca sofware	45
MWB54 ECP for Tb^{III} in Orca software	48
Supplementary note S12 – Python script for the population rates.....	51
References.....	56

Supplementary note S1. Synthesis and characterization

Synthesis of the coordination polymers

The synthesis of the 1D coordination polymers was previously described elsewhere.¹ $[\text{Ln}(\text{tfa})_3(\mu\text{-dppeo})]_n$ (**1**) and $[\text{Ln}(\text{tfa})_3(\mu\text{-dppbo})]_n$ (**2**) ($\text{Ln} = \text{Eu}, \text{Tb}$) were synthesized by dissolving the $[\text{Ln}(\text{tfa})_3(\text{H}_2\text{O})_2]$ precursor (0.2 mmol) in 20 mL of ethanol followed by the addition of the dppeo or dppbo bridge ligand (0.1 mmol). The solution was kept undisturbed for 3 days and after that, white crystals were obtained (yield of 60%). The Eu^{III} to Tb^{III} molar ratio was kept as 1:1 (50% to each other) in both systems. All the measurements were undertaken by employing the crashed crystals.

$[\text{Ln}(\text{tfa})_3(\mu\text{-dppeo})]_n$ (1**)**: FTIR (cm^{-1} , Figure S2): 3064 (w), 2357 (w), 1654 (m), 1635 (s), 1588 (w), 1540 (w), 1517 (m), 1498 (s), 1481 (s), 1457 (m), 1436 (s), 1390 (w), 1356 (m), 1279 (s), 1216 (w), 1197 (m), 1171 (s), 1116 (s), 1081 (m), 1027 (m), 997 (m), 978 (w), 943 (m), 929 (w), 892 (w), 850 (m), 836 (m), 767 (m), 750 (m), 739 (m), 724 (s), 691 (s), 667 (m), 608 (w), 550 (s), 505 (s). Anal. Calcd (%) for $\text{C}_{41}\text{H}_{36}\text{F}_9\text{O}_8\text{P}_2\text{Eu}_{0.5}\text{Tb}_{0.5}$ (1045.10 g mol⁻¹): C, 47.11; H, 3.47. Found: C, 47.24; H, 3.66.

$[\text{Ln}(\text{tfa})_3(\mu\text{-dppbo})]_n$ (2**)**: FTIR (cm^{-1} , Figure S2): 3064 (w), 2357 (w), 1646 (m), 1624 (s), 1590 (w), 1545 (w), 1517 (m), 1480 (s), 1436 (m), 1424 (s), 1401 (w), 1356 (m), 1289 (s), 1212 (w), 1197 (m), 1186 (m), 1169 (s), 1132 (s), 1121 (s), 1004 (m), 1074 (m), 1029 (m), 1001 (m), 945 (m), 924 (w), 846 (w), 836 (m), 780 (m), 767 (m), 741 (m), 730 (s), 691 (s), 679 (m), 606 (w), 554 (s), 531 (s), 503 (s), 481 (s), 458 (w), 417 (w). Anal. Calcd (%) for $\text{C}_{43}\text{H}_{40}\text{F}_9\text{O}_8\text{P}_2\text{Eu}_{0.5}\text{Tb}_{0.5}$ (1073.15 g mol⁻¹): C, 48.12; H, 3.76. Found: C, 47.86; H, 3.33.

Characterization

PXRD (powder X-ray diffraction). PXRD within 5 - 40° was measured using a Shimadzu XRD 7000 (Cu K_α , $\lambda = 1.5418 \text{ \AA}$) diffractometer operating at 40 kV and 30 mA, with scan rate of 0.5° mim⁻¹.

FTIR (Fourier-transform infrared spectroscopy). FTIR of complexes in solid state was recorded in an Agilent Cary 600 Series FTIR Spectrophotometer (660) in the range of 4,000 to 400 cm^{-1} with a resolution of 2 cm^{-1} using an attenuated total reflectance (ATR) accessory.

Elemental analysis. C, H, N, elementary analysis was measured in a model Perkin Elmer CHN2400.

Thermogravimetry. TG analysis for both complexes was undertaken in a TA equipment, SDT Q600 model, under an N_2 atmosphere. The heating rate was set to 10 °C min⁻¹, with approximately 5 mg of sample weighed into an alumina crucible.

PL (photoluminescence). PL were carried out in a Fluorolog-3 spectrofluorometer (Horiba FL3-22-iHR320) with double-gratings (1,200 grooves mm⁻¹, 330 nm blaze) in the excitation monochromator and double-gratings (1200 grooves mm⁻¹, 500 nm blaze) in the emission monochromator. An ozone-free xenon lamp of 450 W (Ushio) was used as a radiation source. A 150 W pulsed xenon lamp was used for time-resolved measurements by using a time-correlated single-photon counting (TCSPC) system. A photomultiplier (Hamamatsu R928P) operating at 950 V was used to collect the spectra in the ultraviolet and visible spectral regions, which were corrected according to the optical system of the emission monochromator and the photomultiplier response. The emission and excitation spectra were carried using the front face mode at 22.51°. The excitation and emission slits were kept in a position to lead to a spectral bandpass of 1 nm in all experiments.

Luminescence thermometry. Emission spectra from 77 K to 430 K were measured in the previously mentioned Fluorolog 3 equipment. The excitation and emission slits were kept in a position to lead to a spectral bandpass of 1 nm in all experiments. To control the temperature, a Linkam accessory (THMS600), with an optical fiber set (NA = 0.22 - Horiba-FL-3000/FM4-3000) was used. The relative thermal sensitivity of the systems was calculated from eqn S1, where Δ is the thermometric parameter and T is the temperature. The thermometric parameter was fitted by using a logistic function (eqn S4). The temperature uncertainty (δT) is calculated by eqn S2 and eqn S3, where $\delta I/I$ is the relative uncertainty in the integrated area.² δI was calculated from the signal-to-noise ratio for each normalized spectrum measured within the 555 – 595 nm spectral range, which was close to 0.01 for all of them. Thus, eqn S3 can be reduced to $\delta I/I = 0.01$ for all spectra considering the normalized spectra since $I_{max} = 1$.

$$S_r = \frac{1}{\Delta} \left| \frac{d\Delta}{dT} \right| \quad (S1)$$

$$\delta T = \frac{1}{S_r \Delta} \delta \Delta \quad (S2)$$

$$\frac{\delta \Delta}{\Delta} = \sqrt{\left(\frac{\delta I_1}{I_1} \right)^2 + \left(\frac{\delta I_2}{I_2} \right)^2} = \sqrt{2} \frac{\delta I}{I} \quad (S3)$$

$$\Delta = A_2 + \frac{A_1 - A_2}{1 + \left(\frac{T}{T_0} \right)^p} \quad (S4)$$

Supplementary note S2. Computational and theoretical details

Computational protocol

All electronic structure calculations within the density functional theory (DFT) and time dependent (TD-DFT) level of theory discussed in the main text and Supporting Information were carried out with the quantum chemistry package Orca 5.0.4³.

Geometry Optimization. In the present work, only the position of the hydrogen atoms was optimized. This is achieved at the DFT level of theory, using the PBE0 functional⁴ along with the D4 dispersion correction⁵. Aiming at an accurate optimization, we employed the Def2-TZVP basis set⁶ with no auxiliary resolution of identity (RI) approximation.

Excited-States calculation and frequency. With the optimized structure of both coordination polymers, a TD-DFT calculation was performed to harness the energies of the singlets and triplets excited states, and its composition in terms of molecular orbitals. With this in mind, we employed the range-separated ωB97x hybrid functional⁷ with the D4 dispersion correction as well⁵. All atoms in the system were described with the same Def2-TZVP basis set, except Eu^{III} and Tb^{III}, as they were described by the Stuttgart-Cologne adapted MWB52 and MWB54 effective core potential (ECP), respectively, along with its Gaussian-type basis set⁸. We highlight that this ECP is widely employed for such calculations, as they allow us to consider the system's multiplicity as a singlet due to the buried nature of the 4f orbitals⁹. The method is therefore written as ωB97x-D4/Def2-TZVP/MWB52(54). After this step, an analytical Hessian calculation was performed to determine the energies of the molecule's vibrational modes at the ground-state using the analogous PBE0-D4/Def2-TZVP/MWB52(54) method.

Theoretical details

This section of the paper includes finding the parameters necessary to understand the roles of energy transfer in the thermometric behavior of both compounds. Within this framework, the ligand-to-lanthanide and lanthanide-to-lanthanide energy transfer rates are determined. The first can be determined using the *JoySpectra* webplatform¹⁰, according to the data extracted from the TD-DFT calculations, while the latter is determined manually using coding scripts.

Theoretical Judd-Ofelt intensity parameters. These parameters are often treated as phenomenological from an experimental perspective; however, their theoretical counterparts furnish crucial information on the chemical environment surrounding the Ln^{III}. For Eu^{III}, they were determined by the fitting procedure detailed elsewhere¹¹. Nevertheless, it is valuable to briefly recall the equations that describe their decomposition into forced-electric dipole (FED, Eq. S6) and dynamic coupling (DC, Eq. S7) components to determine their values for Tb^{III}. In these equations, t and p are the ranks and components of the spherical harmonics (Y_p^t), while ΔE stands for the average energy denominator method¹². The numerical factors $\Theta(t,\lambda)$ are the relation between $f-g$ and $f-d$ interconfigurational transitions and 4f radial integrals¹³, assuming values of $\Theta(1,2) = -0.17$, $\Theta(3,2) = 0.34$, $\Theta(3,4) = 0.18$, $\Theta(5,4) = -0.24$, $\Theta(5,6) = -0.24$, $\Theta(7,6) = 0.24$. g_j is the charge factor, which is essential in this description¹⁴, which together with the overlap integral (ρ_j) compose the overlap charge between the coordinating atom and the Ln^{III}. Also, β_j is described by the by $(1 \pm \beta_j)^{-1}$. Y_p^t represents the spherical harmonics where the site symmetry is treated by the sum over j index. Concerning the dynamic coupling mechanism, $\alpha_{OP,j}$ and α'_j represents the chemical

bond overlap polarizability and the ligand effective polarizability¹⁵, respectively. The latter is pivotal in determining the molecular region that interacts with the Ln^{III}.

$$\Omega_{\lambda}^{theo} = (2\lambda + 1) \sum_{t,p} \frac{|B_{\lambda tp}|^2}{2t + 1}, \quad B_{\lambda tp} = B_{\lambda tp}^{FED} + B_{\lambda tp}^{DC} \quad (S5)$$

$$B_{\lambda tp}^{FED} = \frac{2}{\Delta E} \langle r^{t+1} \rangle \Theta(t, \lambda) \left(\frac{4\pi}{2t + 1} \right)^{1/2} \sum_j \frac{e^2 \rho_j g_j (2\beta_j)^{t+1}}{R_j^{t+1}} (Y_p^{t*})_j \quad (S6)$$

$$B_{\lambda tp}^{DC} = - \left[\frac{(\lambda + 1)(2\lambda + 3)}{(2\lambda + 1)} \right]^{1/2} \langle r^\lambda \rangle \langle f | |C^{(\lambda)}| |f\rangle \left(\frac{4\pi}{2t + 1} \right)^{1/2} \sum_j \frac{[(2\beta_j)^{t+1} \alpha_{op,j} + \alpha'_j]}{R_j^{t+1}} (Y_p^{t*})_j \delta_{t,\lambda+1} \quad (S7)$$

Within this description, we first extracted the g_j and α'_j values of the Eu^{III} ion with the fitting. By comparing the structure of both coordination polymers, i.e., bond lengths and angles, it was reasonable to assume that both Eu^{III} and Tb^{III} were suffering the same influence by the ligand field. With this in mind, we employed in the calculations concerning the Tb^{III} the same g_j and α'_j values of Eu^{III} to obtain the theoretical intensity parameters for the Tb^{III} counterpart.

Intramolecular energy transfer. With the TD-DFT results, combined with the theoretical intensities parameters from the FED mechanism, we were able to calculate the rates of intramolecular energy transfer (IET) from the excited state (S_1 and T_1) of the antenna ligand to the Eu^{III} and Tb^{III} ions. To obtain the rates we considered three main mechanisms, the dipole-dipole (W_{d-d}), dipole-multipole (W_{m-d}), and exchange mechanism (W_{ex}), as written in equations S8 – S10, where S_d^{Ln} , S_λ^{Ln} , S_{ex}^L , and S_{ex}^{Ln} are hidden in equations S11 – S14 for clarity^{16,17,18,19}.

$$W_{d-d} = \frac{2\pi}{\hbar} \left(\frac{S_d^L S_d^{Ln}}{G R_L^6} \right) F \quad (S8)$$

$$W_{d-m} = \frac{2\pi}{\hbar} \left[\frac{S_d^L}{G} \left(\sum_\lambda \frac{S_\lambda^{Ln}}{(R_L^{\lambda+2})^2} \right) \right] F \quad (S9)$$

$$W_{ex} = \frac{2\pi}{\hbar} \left(\frac{S_{ex}^L S_{ex}^{Ln}}{G R_L^4} \right) F \quad (S10)$$

$$S_d^{Ln} = \frac{2e^2(1-\sigma_1)^2}{(2J+1)} \sum_\lambda \Omega_\lambda^{FED} \langle \psi' J' | |U^{(\lambda)}| | \psi J \rangle^2 \quad (S11)$$

$$S_\lambda^{Ln} = \frac{e^2(1-\sigma_\lambda)^2(\lambda+1)}{(2J+1)} \langle r^\lambda \rangle^2 \langle f | |C^{(\lambda)}| |f\rangle^2 \langle \psi' J' | |U^{(\lambda)}| | \psi J \rangle^2 \quad (S12)$$

$$S_{ex}^L = \frac{4(1-\sigma_0)^2}{3(2J+1)} e^2 \langle \psi' J' | |S| | \psi J \rangle^2 \quad (S13)$$

$$S_{ex}^{Ln} = e^2 \sum_m \left| \left\langle \varphi \left| \sum_j \mu_z(j) s_m(j) \right| \varphi * \right\rangle \right|^2 \quad (S14)$$

$$R_L = \frac{\sum_{ij} a_j^2 c_i^2 R_L(i)}{\sum_{ij} a_j^2 c_i^2} \quad (S15)$$

In all equations, R_L represents distance between the donor and acceptor states, which is obtained from the excited state calculation (Eq S15). It is noteworthy that R_L considers the individual distance between the atomic centre and the Ln^{III} ($R_L(i)$, the i -th atomic orbital coefficient contributing to the ligand donor states and incorporates the j -th orbital excitation that composes the excited state. The quantity Ω_λ^{FED} denotes the intensity parameters regarding only the forced electric-dipole contribution. The terms $\langle \psi' J' | |U^{(\lambda)}| | \psi J \rangle^2$ were obtained from reference [20], while the squared spin-operator matrix elements, $\langle \psi' J' | |S| | \psi J \rangle^2$ were calculated using free-ions wave functions within the intermediate coupling scheme^{21, 22} (**Table S1**). S_L corresponds to the dipole strength of the ligand transition involved in the IET process, with values of 10^{-36} and 10^{-40} esu² cm² for S_1 and T_1 , respectively¹⁶. Factor G represents the state degeneracy (equal 1 for S_1 and 3 for T_1), while the shielding factors $(1 - \sigma_k)$ are also considered²³.

For lanthanide-based systems, the IET process is assumed to be non-resonant¹⁶. Consequently, all equations need an energy mismatch factor (F), represented in equation S16. Here we consider that the bandwidth of the ligands ($\gamma_L \approx 3000 \text{ cm}^{-1}$) is much larger than that of the lanthanides ($\gamma_{Ln} \approx 300 \text{ cm}^{-1}$), $\gamma_L \gg \gamma_{Ln}$.¹⁶ The parameter δ represents the maximum energy difference between donor state (D) and the acceptor state of the lanthanide ion, $\delta = E_D - E_{Ln}$. Forward energy transfer (W), therefore, can be obtained by summing all mechanisms (Equation S17)¹⁹.

$$F = \frac{G(\delta, T)}{\hbar \gamma_L} \sqrt{\frac{\ln(2)}{\pi}} e^{-\left(\frac{\delta}{\hbar \gamma_L}\right)^2 \ln(2)}, \text{ with } G(\delta, T) = \begin{cases} 1 & \text{if } \delta \geq 0 \\ e^{\left(\frac{\delta}{k_B T}\right)} & \text{if } \delta < 0 \end{cases} \quad (S16)$$

$$W = W_{d-d} + W_{d-m} + W_{ex} \quad (S17)$$

The backward energy transfer rates (W^b), that is, the energy returned from the acceptor to the donor state, can be obtained using the same equations, where k_B is the Boltzmann constant, with value of $1.3806 \times 10^{-23} \text{ J K}^{-1}$, and T is the temperature.

Lanthanide-to-lanthanide energy transfer. For the rates of lanthanide-to-lanthanide energy transfer, three more aspects besides the ones aforementioned must be considered, i.e., the W_{d-q} , W_{q-q} , W_{md-md} , which represents the dipole-quadrupole, quadrupole-quadrupole, and magnetic dipole interactions^{24,25}. However, one can notice that W_{d-d} also changes its expression. Thus, we highlight their expressions in equations S18 – S22, where S_d^x , S_q^x , and S_{md}^x are hidden in equations S23 – S25 for clarity, in which $x = D$ (donor) or A (acceptor).

$$W_{d-d} = \frac{4\pi}{3\hbar} \left(\frac{S_d^D S_d^A}{R_{DA}^6} \right) F \quad (S18)$$

$$W_{dq-dq} = \frac{\pi}{\hbar} \left(\frac{S_d^D S_q^A + S_q^D S_d^A}{R_{DA}^8} \right) F \quad (S19)$$

$$W_{q-q} = \frac{28\pi}{5\hbar} \left(\frac{S_q^D S_q^A}{R_{DA}^{10}} \right) F \quad (S20)$$

$$W_{md-md} = \frac{4\pi}{3\hbar} \left(\frac{S_{md}^D S_{md}^A}{R_{DA}^6} \right) F \quad (S21)$$

$$W_{ex} = \frac{2\pi}{\hbar} \left[\left(\frac{e^2}{R_{DA}} \right) \rho_{ij}^2 \right] F \quad (S22)$$

$$S_d^x = \frac{e^2 (1 - \sigma_1^x)^2}{2J_x + 1} \sum_{\lambda=2,4,6} \Omega_\lambda^x \langle \psi_x J_x' | |U^{(\lambda)}| | \psi_x J_x \rangle^2 \quad (S23)$$

$$S_q^x = \frac{e^2 (1 - \sigma_2^x)^2}{2J_x + 1} \langle f | |C^{(2)}| |f\rangle^2 \langle r^2 \rangle_x^2 \langle \psi_x J_x' | |U^{(\lambda)}| | \psi_x J_x \rangle^2 \quad (S24)$$

$$S_{md}^x = \frac{\mu_B^2 (1 - \sigma_{md}^x)^2}{2J_x + 1} \langle \psi_x J_x' | |\hat{L} + g_s \hat{S}| | \psi_x J_x \rangle^2 \quad (S25)$$

These equations are analogous to the ones presented in the IET section. The main difference between them are the adaptations required to incorporate the effects acting on each donor-acceptor Ln-Ln pair. As seen in the expression for the ET rates, their magnitude depends on the strength of the dipole-dipole, quadrupole-quadrupole and magnetic-dipole interactions (Eq S23 – S25, respectively)²⁵. The parameters describing these strengths are also analogous to the IET case. For example, Ω_λ^x represents the forced-electric dipole component of the intensity parameter for the donor or activator ($x = D$ or A), while $\langle \psi_x J_x' | |U^{(\lambda)}| | \psi_x J_x \rangle^2$ signifies the square of the doubly reduced matrix elements for the excited and ground state of the donor or acceptor²⁶. $\langle r^t \rangle$ is the expectation value of r^t with respect to the 4f radial wavefunction and the values for $t = 2, 4$, and 6 can be found in reference [27]. An interesting term that is absent in the IET case is the contribution from the magnetic-dipole interaction, which depends on the Bohr magneton (μ_B) and the doubly reduced matrix element of the angular \hat{L} and spin \hat{S} operators ($\langle \psi_x J_x' | |\hat{L} + g_s \hat{S}| | \psi_x J_x \rangle$) calculated in the intermediate coupling scheme^{21,28,29}, with typical values of 0.1–0.6 for states with different L and S terms. Furthermore, one can notice that as the donor-acceptor distance reduces (R_{DA}), the rate of ET increases due to an inverse rate dependence on the distance.

For lanthanide-based systems, the ET process is non-resonant since there is an energy gap between the donor and acceptor energy levels²⁵. Consequently, all equations need a correction factor known as the energy mismatch (F), analogous to the IET case, assuming the unsimplified form detailed in Eq S26 – S27. To rationalize this approach, we highlight that the due to the strong shielding of the 4f electrons, the energy levels of the Ln^{3+} are almost invariant when changing the environment, thus, we can rely on the

energy of $4f$ manifolds reported for LnF_3 with almost no discrepancy. In contrast to the IET case, where the ligand band width was a lot broader than the Ln^{III} , here both donor and acceptor presents the same magnitude. Therefore, for the Tb-Eu donor-acceptor pair, we will consider $\gamma_D = \gamma_A = 350 \text{ cm}^{-1}$, a value that has been used before for $4f$ transitions, yielding reasonable results.

$$F = \frac{\Upsilon}{(\gamma_D^2 + \gamma_A^2)^{1/2}} e^{-(\Delta/\gamma_D)^2 \Gamma} G(\delta, T), \text{ with } \Upsilon = \left(\frac{\ln 2}{\pi} \right)^{1/2} \frac{1}{ch} \quad (S26)$$

$$\Gamma = \left[1 - \frac{1}{1 + (\gamma_D/\gamma_A)^2} \right] \ln 2 \quad (S27)$$

In this work we are interested in the Tb-Eu rates of energy transfer. Therefore, it is worth recalling two important aspects that should be taken into account when calculating the rates. (i) When Eu^{III} is the acceptor, the levels ${}^7F_0, {}^7F_1$ are thermally coupled according to the Boltzmann distribution, which depends on the energy difference between them. In the case of the pathway involving the ${}^5D_0 \rightarrow {}^7F_0$ transition, the J -mixing between the 7F_0 and 7F_2 levels (of the order of 5%) was considered. (ii) When δE is negative, i.e., when the donor state lies below than the acceptor level in energy, the ET rates are multiplied by the

barrier factor $e^{\left(\frac{\delta}{k_B T} \right)}$, as it occurred in the ligand-to-Ln ET. However, the case of pathway nine (energy from the ${}^5D_4 \rightarrow {}^7F_5$ to ${}^5D_1 \rightarrow {}^7F_1$) is an exception to the rule, as this state resonates between the electronic Stark levels.

Multiphonon relaxation. The multiphonon decay rates involves the vibrational deactivation of the excited state by several phonon modes³⁰. In this sense, the rates can be calculated through the energy gap law^{31,32} by using equation S28. In this expression, ΔE is the energy gap in units of cm^{-1} between successive Ln^{III} levels ($J \rightarrow J'$), and $W_0 \approx 10^8 \text{ s}^{-1}$ represents the decay rate extrapolated to zero energy gap ($\Delta E \approx 0$)³³. The quantity α (in units of cm) depends on the material, since it incorporates the mean phonon energy ($\hbar\bar{\omega}$). With this in mind, the Miyakawa-Dexter model was employed³⁴, represented in equation S29. In this case, N accounts for the number of thermally generated phonons, while S is the Huang-Rhys factor whose typical values are in the range of 0.02 – 0.10 for Ln^{III} ions, while n is the thermally averaged phonon occupancy number (Eq S30). Concomitantly with this effect, we can also determine the nonradiative absorption rates from a lower J' to an upper J level using Boltzmann statistics (Eq. S31)³⁵.

$$W_{J' \rightarrow J} = W_0 e^{-|\alpha| \Delta E} \quad (S28)$$

$$\alpha = \frac{1}{\hbar\bar{\omega}} \left[\ln \left(\frac{N}{S(n+1)} \right) - 1 \right] \quad (S29)$$

$$n = \frac{1}{e^{\left(\frac{\hbar\bar{\omega}}{k_B T} \right)} - 1} \quad (S30)$$

$$W_{J' \rightarrow J} = W_{J \rightarrow J'} e^{-\left(\frac{\Delta E}{k_B T} \right)} \quad (S31)$$

The main difficulty using this method for a coordination polymer is to determine the mean phonon energy. In our approach we address this difficulty by using the weighted average of all vibrational frequencies and their intensities. Within this framework the mean phonon energy was determined to be 1572 and 1560 cm⁻¹ for **1** and **2**, respectively.

Rate equations. After computing all process that interferes with the excited state, such as the population, a system of coupled ordinary differential equations (ODEs) was generated and solved numerically by time propagation to obtain the populations of each step in the IET. The set of ODEs, obtained by directly employing Eq. S32, was solved using Radau methods³⁶, as they have been successfully used in previous investigations, delivering reliable results at a feasible computational cost³⁷. Each simulation was conducted over a time interval ranging from 0–50 ms with a step size of 1 μs. By harvesting the population of the emitting level of Eu^{III} and Tb^{III} (⁵D₀ and ⁵D₄, respectively) as a function of temperature, we can understand the temperature influence on the emitting level, that controls the thermometric response. To completely solve the rates, we need to obtain the pumping rate (ϕ), i.e, the rate involved in populating the excited state after excitation. ϕ is directly determined using the absorption cross-section (σ , with value of $\sim 10^{-16}$ cm² for the ligand and $\sim 10^{-20}$ cm² for f-f transitions), the excitation wavelength (λ_{exc}), Planck's constant (h), speed of light (c), and the power density (ρ), assumed as 1 W cm⁻² in the following expression³⁸: $\phi = \sigma p \lambda_{exc} / hc$.

$$\frac{dP_i(t)}{dt} = \sum_{j=1} W_{j \rightarrow i} P_j(t) - \sum_{j=1} W_{i \rightarrow j} P_i(t), i \neq j \quad (S32)$$

Theoretical thermometric parameter. Once the theoretical intensity parameters and the population of the emissive state for each Ln^{III} have been determined, it is possible to calculate the theoretical thermometric parameter. This relation has been previously reported elsewhere [37]. However, in this paper we propose modifications to consider the excitation wavelength, i.e, considering the ligand-to-Ln and Ln-to-Ln energy transfer. The overall radiative rates can be directly harvested from the Judd-Ofelt theory (Eq. S32), by decomposing the rates into their electric and magnetic dipole strengths (Eq. S33 – S35). To perform these calculations, we applied the dataset obtained from the previous one, such as the doubly reduced matrix elements of the angular and spin operator, $\langle l^N \psi J | L + 2S | l^N \psi' J' \rangle$. However, in this step the refractive index n of the medium and the energetic barycentre of the band ($\omega_{J \rightarrow J'}$) needs to be considered. Herein we have chosen the value of 1.5 for n .

$$A_{J \rightarrow J'} = \frac{4e^2(\omega_{J \rightarrow J'})^3}{3\hbar c^3(2J+1)} \left[\frac{n(n^2+2)^2}{9} S_{ed} + n^3 S_{md} \right] \quad (S33)$$

$$S_{ed} = \sum_{\lambda=2,4,6} \Omega_\lambda \langle \psi' J' | |U^{(\lambda)}| | \psi J \rangle^2 \quad (S34)$$

$$S_{md} = \frac{\hbar}{4m_e^2c^2} \langle l^N \psi J | |L + 2S| | l^N \psi' J' \rangle^2 \quad (S35)$$

The emission of interest for the thermometric parameter are the Eu^{III} ⁵D₀→⁷F₄ and Tb^{III} ⁵D₄→⁷F₅ transitions. To accurately determine the theoretical rate of the emission and its temperature dependence, $A_{J \rightarrow J'}$ is normalized by the population of the emissive state (Eq. S36). One can note that P_4 carries the excitation wavelength dependence intrinsically due to its absorption cross-section dependence³⁹.

$$I_{J \rightarrow J'} = A_{J \rightarrow J'} P_4(Ln) \quad (S36)$$

By estimating the intensities of Eu^{III} and Tb^{III} emission, the theoretical thermometric parameter is

therefore the intensities ratio, analogous to the experimental formula $\left(\Delta = \frac{I_{Tb}}{I_{Eu}} \right)$, which is extended in Eq S37.

$$\Delta = \frac{A_{4 \rightarrow 5} P_4(Tb)}{A_{0 \rightarrow 4} P_4(Eu)} = \frac{1}{9} \left(\frac{\omega_{4 \rightarrow 5}}{\omega_{0 \rightarrow 4}} \right)_3 \left(\sum_{\lambda=2,4,6} \frac{\Omega_\lambda \langle 4 | |U^{(\lambda)}| | 5 \rangle^2}{\Omega_4 \langle 0 | |U^{(\lambda)}| | 4 \rangle^2} + \frac{9n^3 \hbar}{4m_e^2 c^2 (n^2 + 2)^2 \Omega_4} \left(\frac{\langle 4 | |L + 2S| | 5 \rangle}{\langle 0 | |U^{(\lambda)}| | 4 \rangle} \right)_2 \right) \frac{P_4(Tb)}{P_4(Eu)} \quad (S37)$$

It is noteworthy from Eq. S36 that only the populations are temperature dependent, since they carry the temperature variation in the energy transfer and multiphonon relaxation rates. Keeping this observation in mind, we show that the relative sensibility of the thermometer (defined in Eq. S1) depends only on the population of the emitting state within this theoretical framework (Eq. S38).

$$S_r = \frac{P_4(Eu)}{P_4(Tb)} \left| \frac{d}{dT} \left(\frac{P_4(Tb)}{P_4(Eu)} \right) \right| \quad (S38)$$

This is an elegant and unreported method that rationalizes this property even in the absence of the rates, meaning that only the populations are necessary to calculate the relative sensitivity, which can be used to predict this property. It is worth noting that the emission band of the Ln^{III} is not being simulated, but only the intensity, which is proportional to Eq. S33. Minor deviations may arise from the different population of Stark levels. Therefore, the normalization procedure for the theoretical thermometric parameter was applied.

Table S1. Values of squared reduced matrix elements for Eu^{III} ion. The values of $\langle \psi' J' | |U^{(\lambda)}| | \psi J \rangle^2$ were taken from ref. [40], while the $\langle \psi' J' | |S| | \psi J \rangle^2$ were calculated in a previous work using reference [21,41].

Transition	Energy / cm ⁻¹	$\langle \psi' J' U^{(2)} \psi J \rangle^2$	$\langle \psi' J' U^{(4)} \psi J \rangle^2$	$\langle \psi' J' U^{(6)} \psi J \rangle^2$	$\langle \psi' J' S \psi J \rangle^2$
$^7F_0 \rightarrow ^7F_2$	1026	0.137	0	0	0
$^7F_0 \rightarrow ^7F_3$	1866	0	0	0	0
$^7F_0 \rightarrow ^7F_4$	2823	0	0.140	0	0
$^7F_0 \rightarrow ^7F_5$	3849	0	0	0	0
$^7F_0 \rightarrow ^7F_6$	4907	0	0	0.145	0
$^7F_0 \rightarrow ^5D_0$	17293	0	0	0	0
$^7F_0 \rightarrow ^5D_1$	19027	0	0	0	0.027
$^7F_0 \rightarrow ^5D_2$	21483	0	0	0	0
$^7F_0 \rightarrow ^5D_3$	24355	0	0	0	0
$^7F_0 \rightarrow ^5L_6$	25325	0	0	0.015	0
$^7F_0 \rightarrow ^5L_7$	26357	0	0	0	0
$^7F_0 \rightarrow ^5G_2$	26392	0	0	0	0
$^7F_0 \rightarrow ^5G_3$	26622	0	0	0	0
$^7F_0 \rightarrow ^5G_4$	26735	0	0	0	0
$^7F_0 \rightarrow ^5G_6$	26752	0	0	0.004	0
$^7F_0 \rightarrow ^5G_5$	26763	0	0	0	0

$^7F_0 \rightarrow ^5L_8$	27244	0	0	0	0
$^7F_0 \rightarrow ^5D_4$	27586	0	0.001	0	0
$^7F_0 \rightarrow ^5L_9$	27960	0	0	0	0
$^7F_0 \rightarrow ^5L_{10}$	28427	0	0	0	0
$^7F_1 \rightarrow ^7F_2$	654	0.052	0	0	0
$^7F_1 \rightarrow ^7F_3$	1494	0.209	0.128	0	0
$^7F_1 \rightarrow ^7F_4$	2451	0	0.174	0	0
$^7F_1 \rightarrow ^7F_5$	3477	0	0.119	0.054	0
$^7F_1 \rightarrow ^7F_6$	4535	0	0	0.377	0
$^7F_1 \rightarrow ^5D_0$	16921	0	0	0	0.117
$^7F_1 \rightarrow ^5D_1$	18655	0.003	0	0	0
$^7F_1 \rightarrow ^5D_2$	21111	0	0	0	0.005
$^7F_1 \rightarrow ^5D_3$	23983	0	0.001	0	0
$^7F_1 \rightarrow ^5L_6$	24953	0	0	0.009	0
$^7F_1 \rightarrow ^5L_7$	25985	0	0	0.018	0
$^7F_1 \rightarrow ^5G_2$	26020	0	0	0	0.013
$^7F_1 \rightarrow ^5G_3$	26250	0	0.001	0	0
$^7F_1 \rightarrow ^5G_4$	26363	0	0	0	0
$^7F_1 \rightarrow ^5G_6$	26380	0	0	0.005	0
$^7F_1 \rightarrow ^5G_5$	26391	0	0	0.010	0
$^7F_1 \rightarrow ^5L_8$	26872	0	0	0	0
$^7F_1 \rightarrow ^5D_4$	27214	0	0	0	0
$^7F_1 \rightarrow ^5L_9$	27588	0	0	0	0
$^7F_1 \rightarrow ^5L_{10}$	28055	0	0	0	0

Table S2. Values of squared reduced matrix elements for Tb^{III} ion. The values of $\langle \psi'J' | |U^{(2)}| | \psi J \rangle^2$ were taken from ref. [40], while the $\langle \psi'J' | |S| | \psi J \rangle^2$ were calculated in this work using references [21,41].

Transition	Energy / cm ⁻¹	$\langle \psi'J' U^{(2)} \psi J \rangle^2$	$\langle \psi'J' U^{(4)} \psi J \rangle^2$	$\langle \psi'J' U^{(6)} \psi J \rangle^2$	$\langle \psi'J' S \psi J \rangle^2$
$^7F_6 \rightarrow ^7F_4$	3315	0.089	0.516	0.266	0
$^7F_6 \rightarrow ^7F_3$	4294	0	0.232	0.413	0
$^7F_6 \rightarrow ^7F_2$	4982	0.048	0.048	0.469	0
$^7F_6 \rightarrow ^7F_1$	5437	0	0	0.376	0
$^7F_6 \rightarrow ^7F_0$	5660	0	0	0.144	0
$^7F_6 \rightarrow ^5D_4$	20444	0.001	0.001	0.001	0
$^7F_6 \rightarrow ^5D_3$	26236	0	0	0.001	0
$^7F_6 \rightarrow ^5G_6$	26423	0.002	0.004	0.116	0.555
$^7F_6 \rightarrow ^5L_{10}$	26971	0	0	0.058	0
$^7F_6 \rightarrow ^5G_5$	27767	0.001	0.002	0.013	0.038
$^7F_6 \rightarrow ^5D_2$	28107	0	0	0	0
$^7F_6 \rightarrow ^5G_4$	28287	0	0	0.009	0
$^7F_6 \rightarrow ^5L_9$	28408	0	0.002	0.045	0
$^7F_6 \rightarrow ^5G_3$	28977	0	0	0.001	0
$^7F_6 \rightarrow ^5L_8$	29190	0	0	0.023	0
$^7F_6 \rightarrow ^5L_7$	29457	0.001	0	0.012	0
$^7F_6 \rightarrow ^5G_2$	29531	0	0	0	0
$^7F_6 \rightarrow ^5L_6$	29670	0	0	0	0.009
$^7F_6 \rightarrow ^5D_1$	30610	0	0	0	0
$^7F_6 \rightarrow ^5D_0$	31224	0	0	0	0

$^7F_6 \rightarrow ^5H_7$	31379	0	0	0	0.010
$^7F_6 \rightarrow ^5H_6$	32891	0	0	0	0.081
$^7F_6 \rightarrow ^5H_5$	33767	0	0	0	0
$^7F_6 \rightarrow ^5H_4$	34339	0	0	0	0
$^7F_6 \rightarrow ^5F_5$	34934	0	0	0	0.165
$^7F_6 \rightarrow ^5H_3$	34936	0	0	0	0
$^7F_6 \rightarrow ^5I_8$	35131	0	0	0	0
$^7F_6 \rightarrow ^5F_4$	35374	0	0	0	0
$^7F_6 \rightarrow ^5F_3$	36550	0	0	0	0
$^7F_6 \rightarrow ^5I_7$	36589	0	0	0	0.007
$^7F_6 \rightarrow ^5F_2$	37136	0	0	0	0
$^7F_6 \rightarrow ^5F_1$	37482	0	0	0	0
$^7F_6 \rightarrow ^5I_6$	37598	0	0	0	0.106
$^7F_6 \rightarrow ^5I_4$	37608	0	0	0	0
$^7F_6 \rightarrow ^5I_5$	37986	0	0	0	0.009
$^7F_6 \rightarrow ^5K_9$	39173	0	0	0	0
$^7F_6 \rightarrow ^5K_8$	40815	0	0	0	0
$^7F_6 \rightarrow ^5K_5$	41334	0	0	0	0
$^7F_6 \rightarrow ^5K_7$	41693	0	0	0	0
$^7F_5 \rightarrow ^7F_4$	1267	0.554	0.012	0.437	0
$^7F_5 \rightarrow ^7F_3$	2246	0.177	0.250	0.382	0
$^7F_5 \rightarrow ^7F_2$	2934	0	0.314	0.207	0
$^7F_5 \rightarrow ^7F_1$	3389	0	0.119	0.054	0
$^7F_5 \rightarrow ^7F_0$	3612	0	0	0	0
$^7F_5 \rightarrow ^7D_4$	18396	0.014	0.001	0.002	0.051
$^7F_5 \rightarrow ^5D_3$	24188	0.001	0.003	0.002	0
$^7F_5 \rightarrow ^5G_6$	24375	0.004	0.003	0.009	0.073
$^7F_5 \rightarrow ^5L_{10}$	24923	0	0	0.002	0
$^7F_5 \rightarrow ^5G_5$	25719	0	0	0.006	0.243
$^7F_5 \rightarrow ^5D_2$	26059	0	0.003	0.001	0
$^7F_5 \rightarrow ^5G_4$	26239	0.001	0	0.002	0.031
$^7F_5 \rightarrow ^5L_9$	26360	0	0.001	0.014	0
$^7F_5 \rightarrow ^5G_3$	26929	0	0	0	0
$^7F_5 \rightarrow ^5L_8$	27142	0	0.002	0.021	0
$^7F_5 \rightarrow ^5L_7$	27409	0	0	0.007	0
$^7F_5 \rightarrow ^5G_2$	27483	0	0	0	0
$^7F_5 \rightarrow ^5L_6$	27622	0	0	0	0.001
$^7F_5 \rightarrow ^5D_1$	28562	0	0	0	0
$^7F_5 \rightarrow ^5D_0$	29176	0	0	0	0
$^7F_5 \rightarrow ^5H_7$	29331	0	0	0	0
$^7F_5 \rightarrow ^5H_6$	30843	0	0	0	0.010
$^7F_5 \rightarrow ^5H_5$	31719	0	0	0	0.130
$^7F_5 \rightarrow ^5H_4$	32291	0	0	0	0.297
$^7F_5 \rightarrow ^5F_5$	32886	0	0	0	0.172
$^7F_5 \rightarrow ^5H_3$	32888	0	0	0	0
$^7F_5 \rightarrow ^5I_8$	33083	0	0	0	0
$^7F_5 \rightarrow ^5F_4$	33326	0	0	0	0.520
$^7F_5 \rightarrow ^5F_3$	34502	0	0	0	0
$^7F_5 \rightarrow ^5I_7$	34541	0	0	0	0
$^7F_5 \rightarrow ^5F_2$	35088	0	0	0	0
$^7F_5 \rightarrow ^5F_1$	35434	0	0	0	0

$^7F_5 \rightarrow ^5I_6$	35550	0	0	0	0.016
$^7F_5 \rightarrow ^5I_4$	35560	0	0	0	0
$^7F_5 \rightarrow ^5I_5$	35938	0	0	0	0.001
$^7F_5 \rightarrow ^5K_9$	37125	0	0	0	0
$^7F_5 \rightarrow ^5K_8$	38767	0	0	0	0
$^7F_5 \rightarrow ^5K_5$	39286	0	0	0	0
$^7F_5 \rightarrow ^5K_7$	39645	0	0	0	0

Table S3. Values of squared reduced matrix elements for Tb^{III} ion used in the Ln-Ln energy transfer. The values of $\langle \psi' J' | |U^{(\lambda)}| | \psi J \rangle^2$ were taken from ref. [40], while the $\langle \psi' J' | |L + gS| | \psi J \rangle^2$ were calculated in this work according to reference [21,41].

Tb ^{III}	Energy / cm ⁻¹	$\langle \psi' J' U^{(2)} \psi J \rangle^2$	$\langle \psi' J' U^{(4)} \psi J \rangle^2$	$\langle \psi' J' U^{(6)} \psi J \rangle^2$	$\langle \psi' J' L + gS \psi J \rangle^2$
$^5D_4 \rightarrow ^7F_6$	20444	0.0009	0.0008	0.0013	0
$^5D_4 \rightarrow ^7F_5$	18396	0.0142	0.0013	0.0022	0.1618
$^5D_4 \rightarrow ^7F_4$	17129	0.0002	0.0022	0.0014	0.0620
$^5D_4 \rightarrow ^7F_3$	16145	0.0022	0.0005	0.0006	0.6835

Supplementary note S3 – Experimental structural characterization

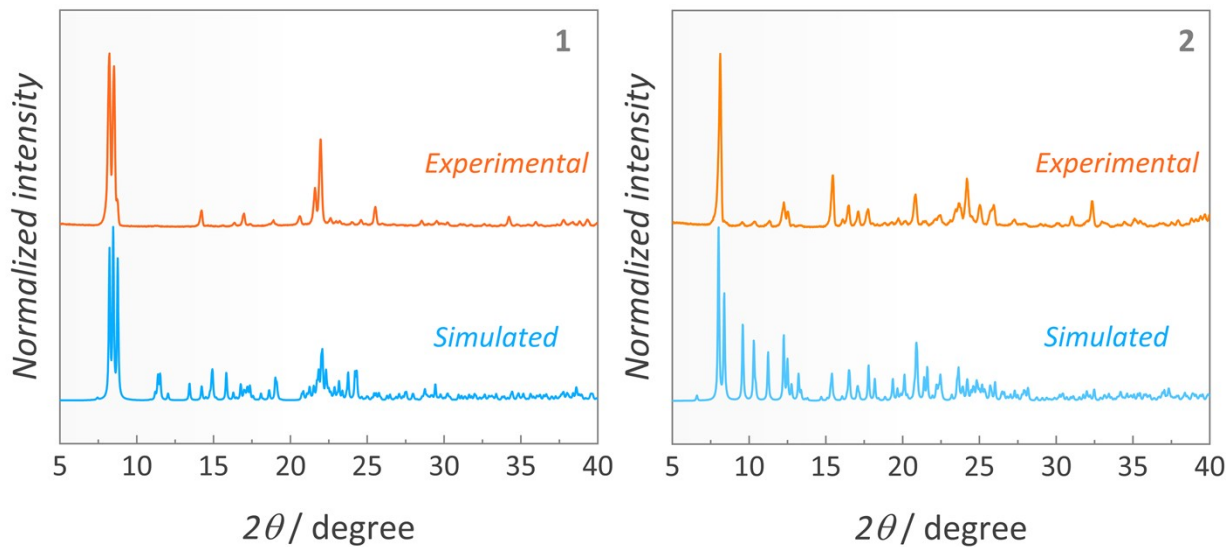


Figure S1. Powder XRD of crashed crystals of **1** and **2** compared to the simulated pattern determined from the SC-XRD previously reported by us elsewhere¹ (CCDC code 2219225 and 2219224). **1** = $[\text{Ln}(\text{tfa})_3(\mu\text{-dppeo})]_n$; **2** = $[\text{Ln}(\text{tfa})_3(\mu\text{-dppbo})]_n$ ($\text{Ln} = \text{Eu, Tb}$). The peaks in the experimental PXRD matches the ones simulated from the SC-XRD analysis. Although the crystals were crashed before undertaking the PXRD data, the crystals were obtained as needles, which presents preferential growth in a specific crystallographic direction. Moreover, needles can also assume a preferential orientation in the sample holder. These effects can lead to changes in the relative peak intensity of the experimental PXRD (measured as a crashed crystal) compared to the PXRD simulated from the SC-XRD analysis (measured for the needle-shaped crystals).⁴² These changes in the relative intensity of the peaks are mainly observed for **2**.

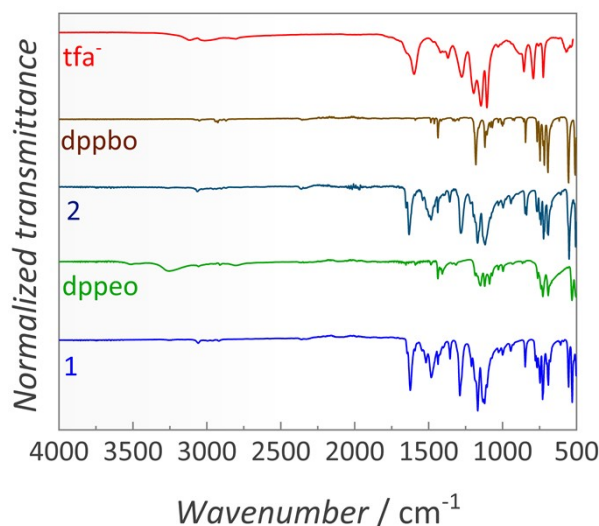


Figure S2. FTIR spectra of **1** and **2** compared to the dppeo, dppbo, and tfa⁻ ligands. **1** = $[\text{Ln}(\text{tfa})_3(\mu\text{-dppeo})]_n$; **2** = $[\text{Ln}(\text{tfa})_3(\mu\text{-dppbo})]_n$ ($\text{Ln} = \text{Eu, Tb}$).

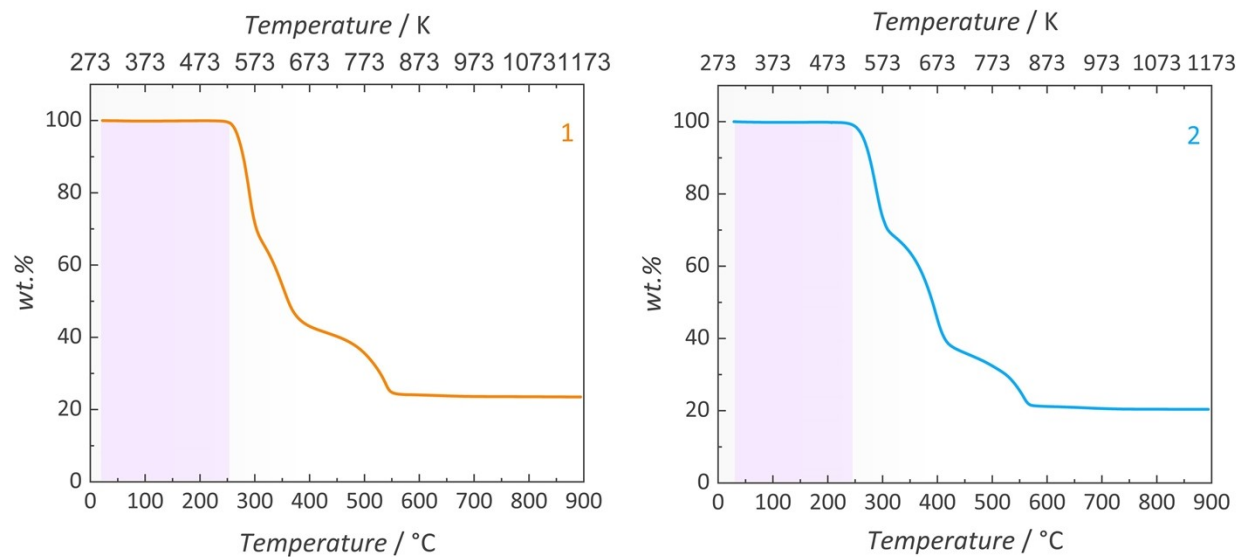


Figure S3. Thermogravimetric analyses (TG) of **1** and **2**. The thermal events after 250 °C correspond to the β -diketone decomposition and the bridge ligand thermolysis. Moreover, after 600 °C, the plateau in the TG curves corresponds to Eu_2O_3 and Tb_4O_7 formation. The residual mass is in accordance with the expected theoretical value for **1** (18%) and **2** (17%). **1** = $[\text{Ln}(\text{tfa})_3(\mu\text{-dppeo})]_n$; **2** = $[\text{Ln}(\text{tfa})_3(\mu\text{-dppbo})]_n$ (Ln = Eu, Tb).

Supplementary note S4 – Additional experimental photoluminescence data

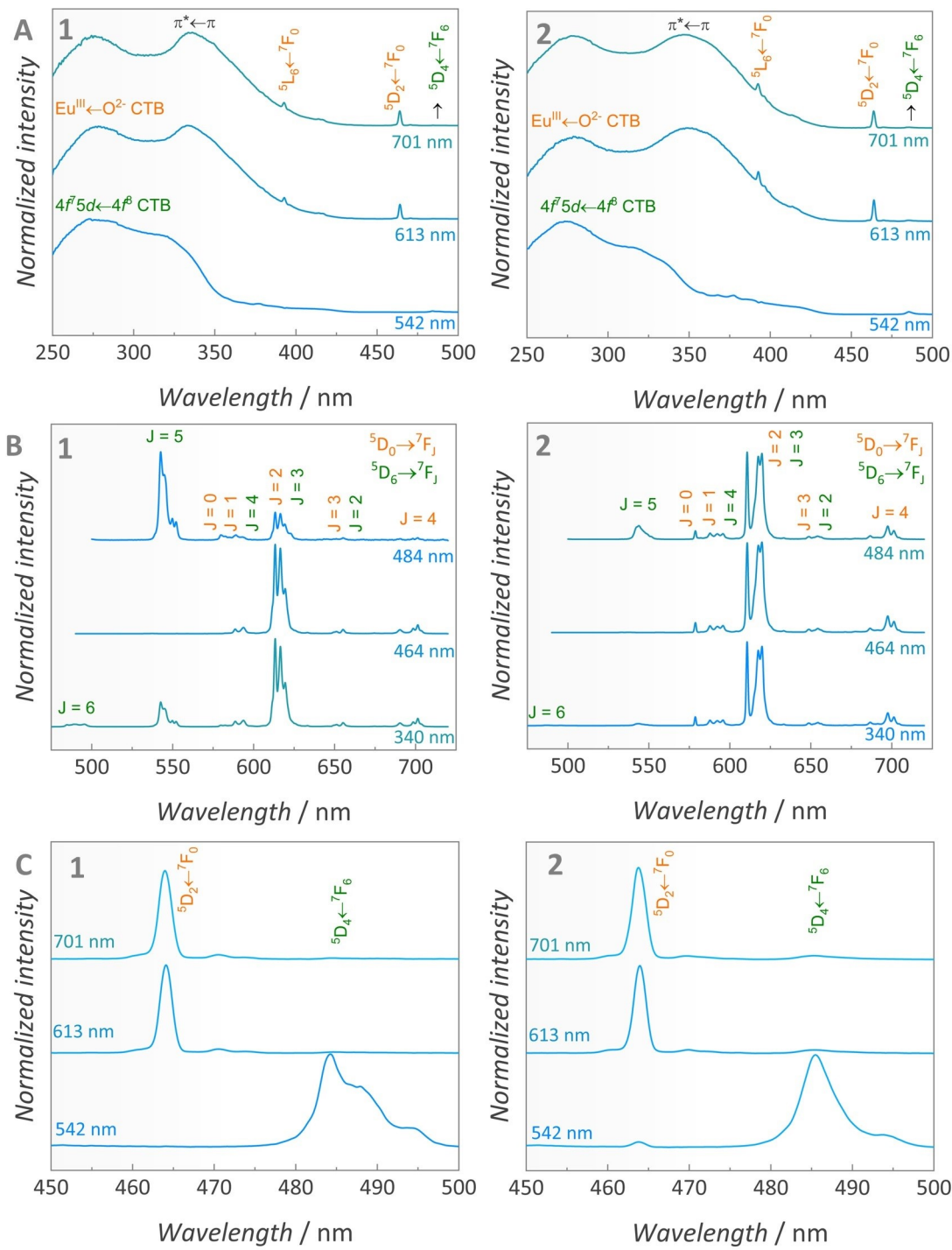


Figure S4. Selective (a) excitation and (b) emission spectra of **1** and **2** measured at 298 K. (c) Magnification of the excitation spectra within the 450 – 500 nm range. The monitored excitation or emission wavelength is displayed in the spectra. Tb^{III} transition assignments are shown in green and Eu^{III} ones in orange. **1** = [Ln(tfa)₃(μ-dppeo)]_n; **2** = [Ln(tfa)₃(μ-dppbo)]_n (Ln = Eu, Tb).

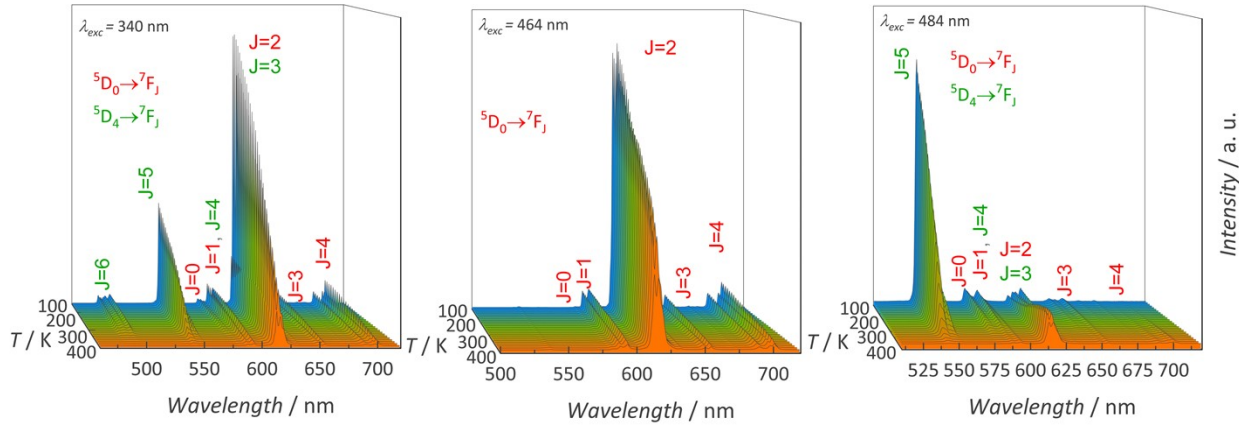


Figure S5. Temperature-dependent emission spectra of **1** under different excitation wavelengths. **1** = $[\text{Ln}(\text{tfa})_3(\mu\text{-dppeo})]_n$ ($\text{Ln} = \text{Eu}, \text{Tb}$).

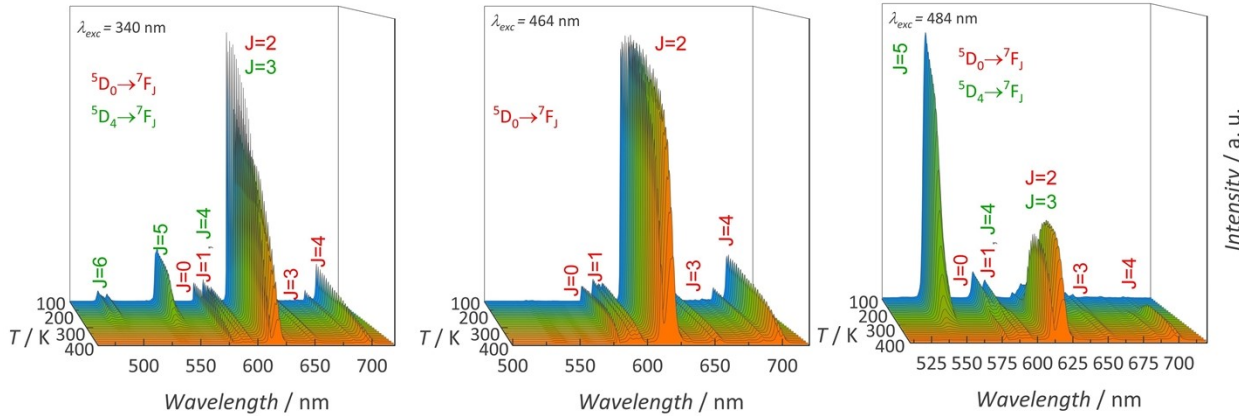
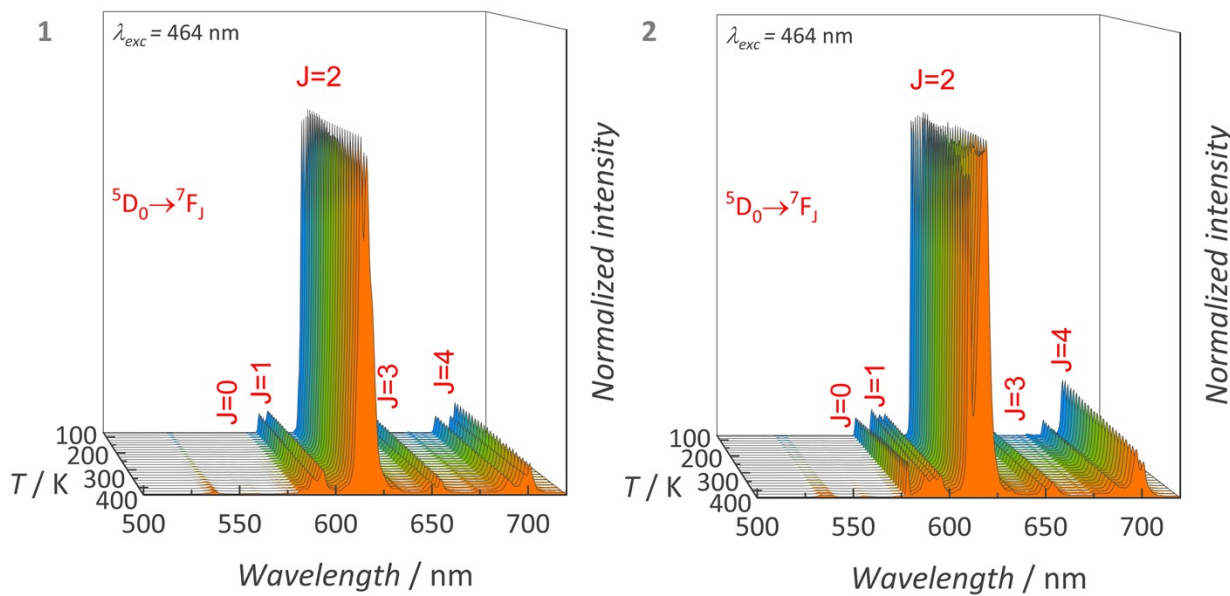
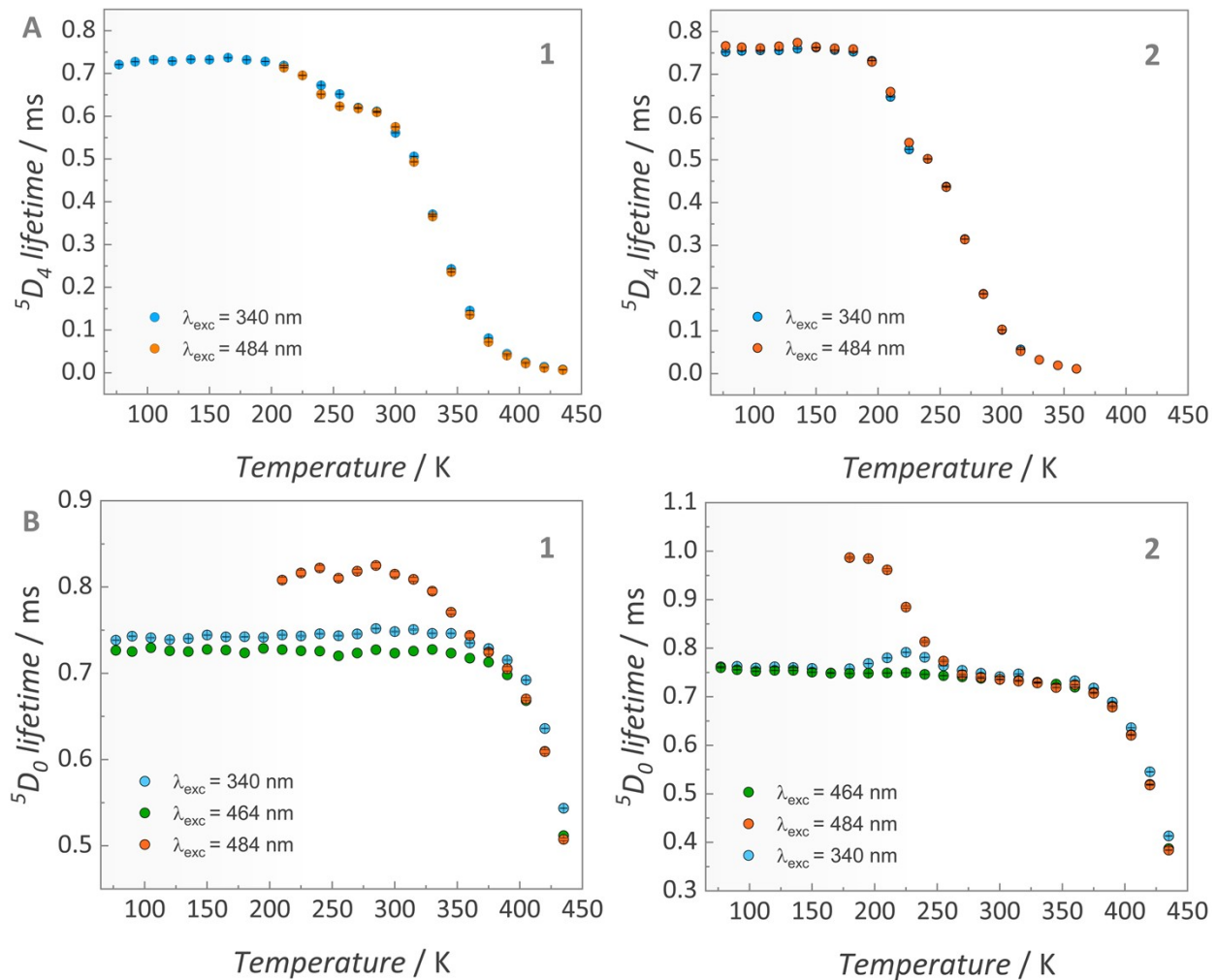


Figure S6. Temperature-dependent emission spectra of **2** under different excitation wavelengths. **2** = $[\text{Ln}(\text{tfa})_3(\mu\text{-dppbo})]_n$ ($\text{Ln} = \text{Eu}, \text{Tb}$).





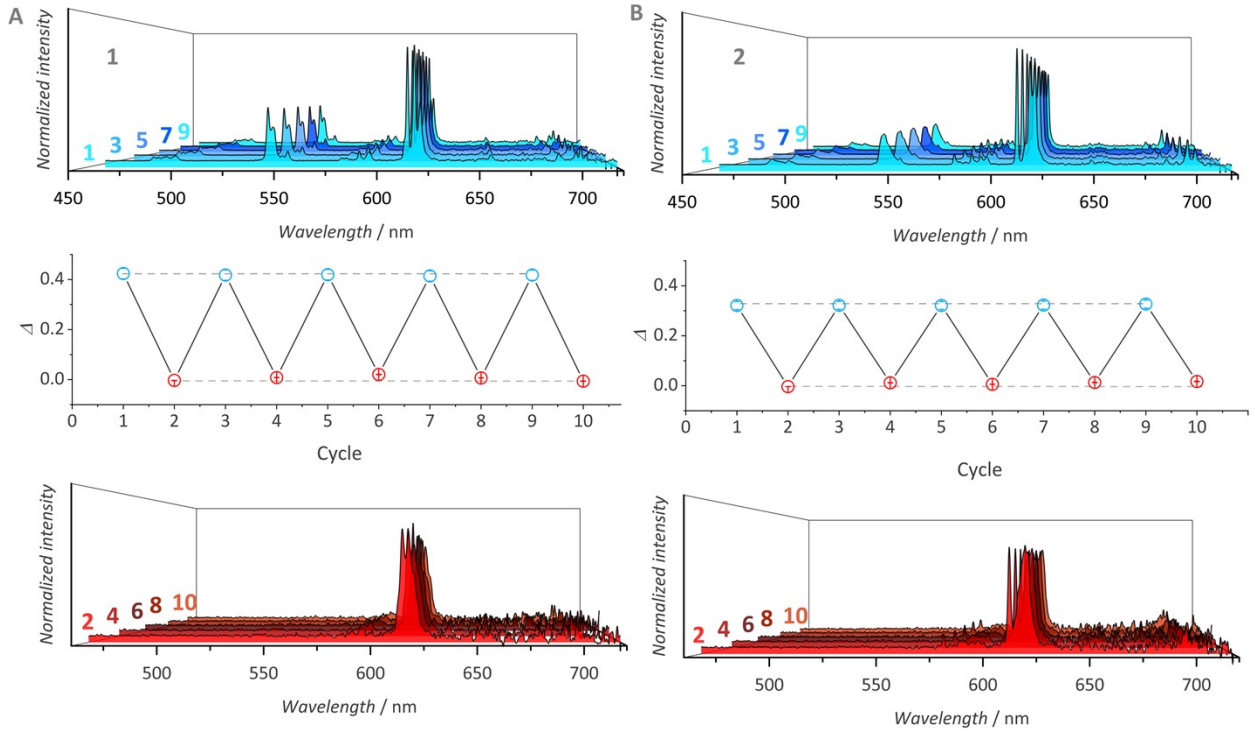


Figure S9. Thermometric parameter ($\lambda_{\text{exc}} = 340 \text{ nm}$) recorded in 10 heating–cooling temperature cycles for (a) **1** and (b) **2**. $\Delta = I_{\text{Tb}}/I_{\text{Eu}}$, where I_{Tb} is the area above the $\text{Tb}^{\text{III}} {}^5\text{D}_4 \rightarrow {}^7\text{F}_5$ transition band (530 - 570 nm) while I_{Eu} is the area above the $\text{Eu}^{\text{III}} {}^5\text{D}_0 \rightarrow {}^7\text{F}_2$ transition (605 - 635 nm, with some contribution of Tb^{III} , overlapped ${}^5\text{D}_4 \rightarrow {}^7\text{F}_3$ band). The bottom and top of each figure represent the emission spectra collected in each cycle. The repeatability (R) of a thermometer’s readout upon temperature cycling is quantified by Equation S39, where Δ_c is the mean thermometric parameter (extracted from the repeatability curve) and Δ_i is the value of each measurement of the thermometric parameter. Both systems present repeatability (R) higher than 99.2%.

$$R = 1 - \frac{\max|\Delta_c - \Delta_i|}{\Delta_c} \quad (\text{S39})$$

Supplementary Note S5. Electronic structure and photophysical parameters of Ln^{III} -based compounds

The time-dependent density functional theory (TD-DFT) calculation was used to acquire the distance between the ligand's centroid position and the Ln^{III} . This quantity allows us to estimate the rates of intramolecular energy transfer from the antenna ligand to the Ln^{III} . However, information such as the forced electric dipole component of the Judd-Ofelt intensity parameters is still required, which can be determined using the same geometry as the one used in the TD-DFT. Thus, in this section we summarize by parts each step of the calculation and its role in the overall mechanism.

Electronic structure

Starting from the electronic structure of both coordination polymers, the outcomes from the TD-DFT calculation are illustrated in Fig S10 – S11.

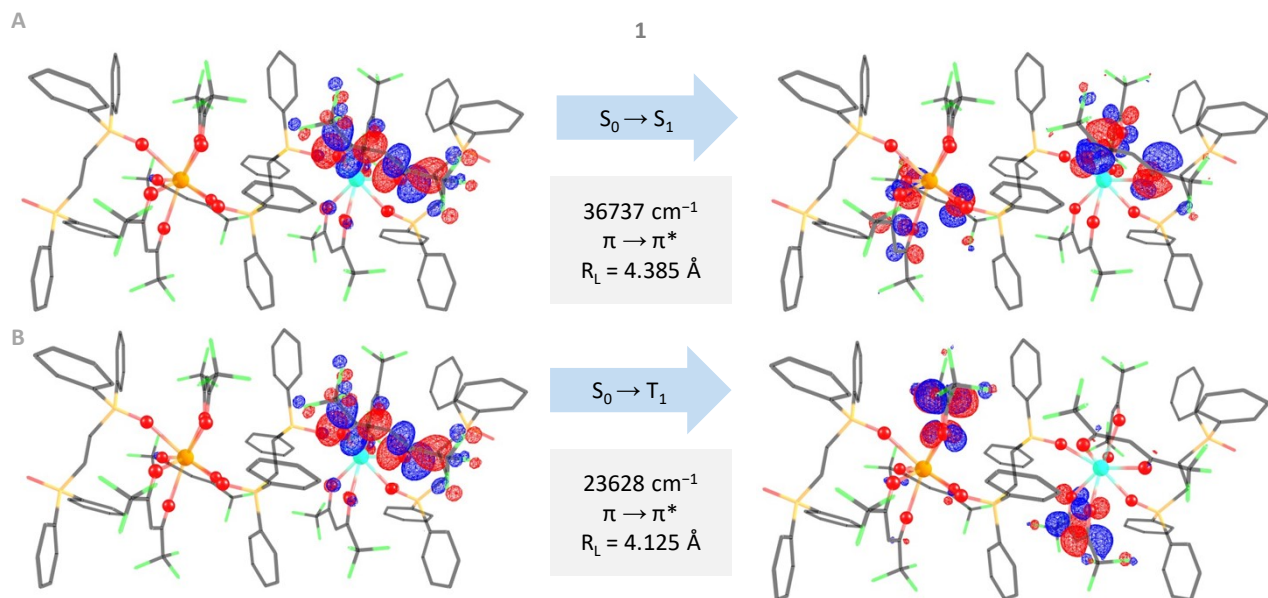


Fig S10. Monoelectronic states involved in the (a) singlet-singlet and (b) singlet-triplet excitation transitions for **1**. Green = fluorine, grey = carbon, orange = europium, cyan = terbium, bright orange = phosphorus, red = oxygen. **1** = $[\text{Ln}(\text{tfa})_3(\mu\text{-dppeo})]_n$ ($\text{Ln} = \text{Eu}, \text{Tb}$). It should be mentioned that the excited states (S_1 and T_1) are a combination of different transitions and different molecular orbitals, and we chose to represent only the molecular orbital with the highest contribution for the S_1/T_1 .

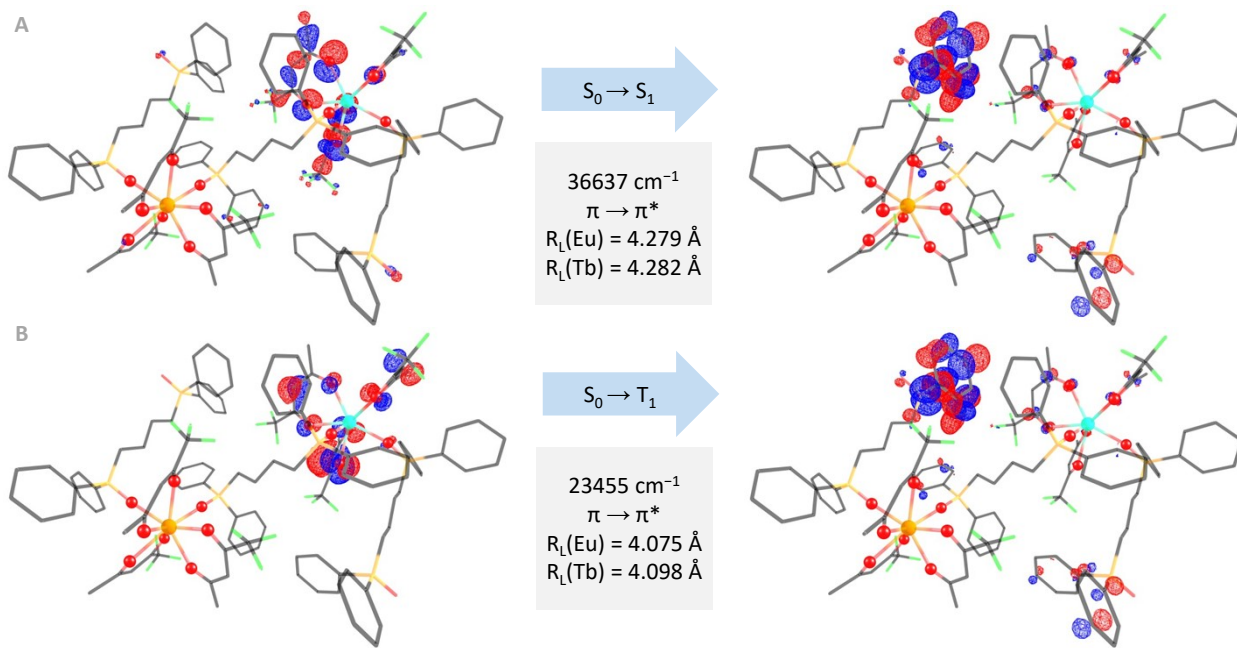


Fig S11. Monoelectronic states involved in the (a) singlet-singlet and (b) singlet-triplet excitation transitions for **2**. Green = fluorine, grey = carbon, orange = europium, cyan = terbium, bright orange = phosphorus, red = oxygen. **2** = $[\text{Ln}(\text{tfa})_3(\mu\text{-dppbo})]_n$ ($\text{Ln} = \text{Eu}, \text{Tb}$). The excited states (S_1 and T_1) are formed by a combination of different molecular orbitals and transitions, and we chose to represent only the molecular orbital with the highest contribution for the S_1/T_1 .

Photophysical parameters

The determination of the experimental Judd-Ofelt intensity parameters for Eu^{III} is quite straightforward from the emission spectrum. However, for Tb^{III} this is not true, as a high contribution from the magnetic dipole strength is observed, inhibiting their direct determination from the emission spectrum. Thus, in this paper we determined the experimental parameters for Eu^{III} , then calculate the theoretical ones using the Monte-Carlo fitting algorithm to extract the ligand field parameters and use the same parameters to calculate the intensity parameters of the Tb^{III} counterpart. In this sense, Tables S4 – S6 were obtained. The parameters considering only the forced-electric dipole were used to harvest the IET pathways, since they are accounted for the dipole-dipole strength. For further information regarding the protocol to calculate the rates, proceed to supplementary note S2 – Intramolecular energy transfer.

Table S4. Experimental and theoretical Judd-Ofelt intensity parameters for the Eu^{III} component of each coordination polymer. All values are in the order of $\times 10^{-20} \text{ cm}^2$. **1** = $[\text{Ln}(\text{tfa})_3(\mu\text{-dppeo})]_n$; **2** = $[\text{Ln}(\text{tfa})_3(\mu\text{-dppbo})]_n$ ($\text{Ln} = \text{Eu}, \text{Tb}$).

Compound	$\Omega_2^{(\text{exp})}$	$\Omega_2^{(\text{theo})}$	$\Omega_4^{(\text{exp})}$	$\Omega_4^{(\text{theo})}$	$\Omega_6^{(\text{theo})}$
1	25.87	25.87	6.150	6.470	0.820
2	23.25	23.24	7.090	7.080	1.650

Table S5. Values of bond length (R_j), charge factor (g_j), effective polarizability (α_j), and bond overlap polarizability ($\alpha_{OP,j}$) for each atom in the Eu^{III} coordination polyhedron derived by the Adaptive Guided Stochastic optimization algorithm. The quantities g_j and α_j were employed for the determination of the Judd-Ofelt parameters for the Tb^{III} counterpart. **1** = [Ln(tfa)₃(μ-dppeo)]_n; **2** = [Ln(tfa)₃(μ-dppbo)]_n (Ln = Eu, Tb).

1	$R_j / \text{\AA}$	g_j	α_j	$\alpha_{OP,j} / \times 10^{-26} \text{ cm}^3$
O(18)	2.327	0.347	0.925	4.231
O(26)	2.312	0.243	0.050	4.349
O(27)	2.392	0.502	2.287	3.769
O(28)	2.376	0.312	0.050	3.879
O(29)	2.402	0.248	0.066	3.700
O(30)	2.402	0.289	0.155	3.703
O(31)	2.392	0.441	0.200	3.767
O(32)	2.401	0.293	0.050	3.705
2				
O(2)	2.300	0.288	0.812	4.434
O(3)	2.347	0.460	0.493	4.082
O(4)	2.395	0.303	0.133	3.752
O(5)	2.408	0.327	0.136	3.663
O(6)	2.380	0.349	0.164	3.850
O(7)	2.411	0.329	0.149	3.640
O(8)	2.355	0.340	1.045	4.026
O(9)	2.379	0.431	1.857	3.855

Table S6. Decomposition of the theoretical intensity parameters into their forced electric dipole (FED) and dynamic coupling (DC) counterparts for both coordination polymers. The decomposition follows the procedure reported in the Theoretical Judd-Ofelt Parameters of Supplementary Note S2. All $\Omega_{2,4,6}$ are in 10^{-20} cm^2 units. **1** = [Ln(tfa)₃(μ-dppeo)]_n; **2** = [Ln(tfa)₃(μ-dppbo)]_n (Ln = Eu, Tb).

Compound	Intensity parameters					
	$\Omega_{2}^{(FED)}$	$\Omega_{2}^{(DC)}$	$\Omega_{4}^{(FED)}$	$\Omega_{4}^{(DC)}$	$\Omega_{6}^{(FED)}$	$\Omega_{6}^{(DC)}$
1						
Eu ^{III}	0.00595	25.26	0.0589	5.324	0.104	0.512
Tb ^{III}	0.0141	25.47	0.0922	4.754	0.157	0.371
2						
Eu ^{III}	0.00520	22.75	0.0657	5.817	0.135	1.093
Tb ^{III}	0.00695	18.11	0.0406	4.517	0.0813	0.725

Supplementary note S6. Intramolecular energy transfer (Ligand-to-Ln^{III})

Employing equations S8 – S16, we were able to determine the rates of intramolecular energy transfer, after computing the forced-electric dipole counterpart of the Judd-Ofelt parameters. To decompose the rates for each Ln^{III} separately, calculations were performed for each moiety. In the case of **2**, where distinct values of R_L were found for Tb^{III} and Eu^{III}, the corresponding value for each Ln^{III} was used (Fig S11).

Table S7. Energy transfer rates (in s⁻¹) for **1** considering the ligand-to-Eu^{III} process. δ is the donor-acceptor (singlet/triplet-Eu^{III}) energy difference (in cm⁻¹). We summarize in this table only the pathways contributing more than 0.001% of the total 40 pathways (1 – 40). W_{d-d} , W_{m-d} , W_{ex} are the dipole-dipole, dipole-multipole, and exchange rates, respectively. W and W^b are the total forward and backward energy transfer rates (sum of each component), respectively at 300.15 K. **1** = [Ln(tfa)₃(μ-dppeo)]_n (Ln = Eu, Tb).

Pathway	Donor	Acceptor	δ	W_{d-d}	W_{m-d}	W_{ex}	W	W_b
7	S ₁	⁷ F ₀ → ⁵ D ₁	17710	0	0	1.522×10 ³	1.522×10 ³	7.905×10 ⁻³⁵
10	S ₁	⁷ F ₀ → ⁵ L ₆	11412	1.254×10 ³	9.212×10 ¹	0	1.346×10 ³	2.116×10 ⁻²²
15	S ₁	⁷ F ₀ → ⁵ G ₆	9985	1.138×10 ³	8.362×10 ¹	0	1.222×10 ³	1.802×10 ⁻¹⁹
18	S ₁	⁷ F ₀ → ⁵ D ₄	9151	3.803×10 ³	5.973×10 ³	0	6.354×10 ³	7.388×10 ⁻¹⁷
26	S ₁	⁷ F ₁ → ⁵ D ₀	19816	0	0	1.430×10 ¹	1.430×10 ¹	1.361×10 ⁻³⁹
27	S ₁	⁷ F ₁ → ⁵ D ₁	18082	1.560×10 ⁻⁴	1.168×10 ¹	5.920×10 ⁻²	1.174×10 ¹	1.522×10 ⁻³⁶
28	S ₁	⁷ F ₁ → ⁵ D ₂	15626	0	0	3.484×10 ²	3.484×10 ²	3.356×10 ⁻³⁰
29	S ₁	⁷ F ₁ → ⁵ D ₃	12754	9.448×10 ⁻¹	2.318×10 ³	0	2.319×10 ³	1.613×10 ⁻²³
30	S ₁	⁷ F ₁ → ⁵ L ₆	11784	3.453×10 ¹	2.537×10 ⁰	0	3.707×10 ¹	1.455×10 ⁻²³
31	S ₁	⁷ F ₁ → ⁵ L ₇	10752	1.881×10 ²	1.382×10 ¹	0	2.019×10 ²	9.691×10 ⁻²¹
32	S ₁	⁷ F ₁ → ⁵ G ₂	10717	0	0	2.639×10 ⁵	2.639×10 ⁵	4.493×10 ⁻¹⁷
33	S ₁	⁷ F ₁ → ⁵ G ₃	10487	9.109×10 ⁰	1.143×10 ⁴	0	1.144×10 ⁴	4.193×10 ⁻¹⁸
35	S ₁	⁷ F ₁ → ⁵ G ₅	10357	7.309×10 ¹	5.368×10 ⁰	0	7.845×10 ¹	2.888×10 ⁻²⁰
36	S ₁	⁷ F ₁ → ⁵ G ₆	10346	1.495×10 ²	6.400×10 ¹	0	2.135×10 ²	9.792×10 ⁻²⁰
Total							2.890×10⁵	1.233×10⁻¹⁶
7	T ₁	⁷ F ₀ → ⁵ D ₁	4601	0	0	3.162×10 ⁸	3.162×10 ⁸	3.308×10 ⁻²
26	T ₁	⁷ F ₁ → ⁵ D ₀	6707	0	0	3.250×10 ⁷	3.250×10 ⁷	6.225×10 ⁻⁶
27	T ₁	⁷ F ₁ → ⁵ D ₁	4973	3.644×10 ⁻³	3.082×10 ²	1.877×10 ⁴	1.908×10 ⁴	4.981×10 ⁻⁶
28	T ₁	⁷ F ₁ → ⁵ D ₂	2517	0	0	6.787×10 ⁶	6.787×10 ⁶	1.387×10 ²
32	T ₁	⁷ F ₁ → ⁵ G ₂	-2392	0	0	2.029×10 ²	2.029×10 ²	6.959×10 ⁷
Total							3.555×10⁸	6.959×10⁷

Table S8. Energy transfer rates (in s^{-1}) for **1** considering the ligand-to-Tb^{III} process. δ is the donor-acceptor (singlet/triplet-Eu^{III}) energy difference (in cm^{-1}). We summarize in this table only the pathways contributing more than 0.001% of the total 78 pathways (1 – 78). W_{d-d} , W_{m-d} , W_{ex} are the dipole-dipole, dipole-multipole, and exchange rates, respectively. W and W^b are the total forward and backward energy transfer rates (sum of each component), respectively at 300.15 K. **1** = $[Ln(tfa)_3(\mu\text{-dppeo})]_n$ ($Ln = Eu, Tb$).

Pathway	Donor	Acceptor	δ	W_{d-d}	W_{m-d}	W_{ex}	W	W_b
8	S ₁	$^7F_6 \rightarrow ^5G_6$	10314	4.539×10^3	1.419×10^5	2.647×10^7	2.662×10^7	8.765×10^{-8}
10	S ₁	$^7F_6 \rightarrow ^5G_5$	8970	1.676×10^3	3.262×10^5	5.586×10^6	5.913×10^6	1.450×10^{-12}
12	S ₁	$^7F_6 \rightarrow ^5G_4$	8450	1.546×10^3	4.036×10^4	0	4.191×10^4	1.512×10^{-13}
16	S ₁	$^7F_6 \rightarrow ^5L_7$	7280	4.716×10^3	5.350×10^5	1.879×10^2	5.399×10^5	3.214×10^{-10}
18	S ₁	$^7F_6 \rightarrow ^5L_6$	7067	0	0	4.992×10^6	4.992×10^6	9.391×10^{-9}
21	S ₁	$^7F_6 \rightarrow ^5H_7$	5358	0	0	1.377×10^7	1.377×10^7	8.259×10^{-5}
22	S ₁	$^7F_6 \rightarrow ^5H_6$	3846	0	0	2.030×10^8	2.030×10^8	1.981×10^0
25	S ₁	$^7F_6 \rightarrow ^5F_5$	1803	0	0	6.859×10^8	6.859×10^8	1.424×10^5
30	S ₁	$^7F_6 \rightarrow ^5I_7$	148	0	0	3.490×10^7	3.490×10^7	1.488×10^7
33	S ₁	$^7F_6 \rightarrow ^5I_6$	-861	0	0	7.907×10^6	7.907×10^6	4.913×10^8
35	S ₁	$^7F_6 \rightarrow ^5I_5$	-1249	0	0	1.000×10^5	1.000×10^5	4.721×10^7
47	S ₁	$^7F_5 \rightarrow ^5G_6$	12362	6.831×10^1	5.585×10^4	5.496×10^5	6.055×10^5	9.151×10^{-21}
49	S ₁	$^7F_5 \rightarrow ^5G_5$	11018	1.562×10^2	5.460×10^3	7.147×10^6	7.153×10^6	8.048×10^{-17}
51	S ₁	$^7F_5 \rightarrow ^5G_4$	10498	8.210×10^1	4.418×10^4	1.471×10^6	1.515×10^6	2.523×10^{-16}
55	S ₁	$^7F_5 \rightarrow ^5L_7$	9328	7.104×10^2	4.839×10^4	0	4.910×10^4	1.342×10^{-15}
57	S ₁	$^7F_5 \rightarrow ^5L_6$	9115	0	0	1.887×10^5	1.887×10^5	1.652×10^{-14}
61	S ₁	$^7F_5 \rightarrow ^5H_6$	5894	0	0	1.306×10^7	1.306×10^7	5.850×10^{-6}
62	S ₁	$^7F_5 \rightarrow ^5H_5$	5018	0	0	2.470×10^8	2.470×10^8	8.730×10^{-3}
63	S ₁	$^7F_5 \rightarrow ^5H_4$	4446	0	0	7.135×10^8	7.135×10^8	4.788×10^{-1}
64	S ₁	$^7F_5 \rightarrow ^5F_5$	3851	0	0	5.117×10^8	5.117×10^8	4.875×10^0
67	S ₁	$^7F_5 \rightarrow ^5F_4$	3411	0	0	1.777×10^9	1.777×10^9	1.707×10^2
72	S ₁	$^7F_5 \rightarrow ^5I_6$	1187	0	0	8.461×10^7	8.461×10^7	2.413×10^5
74	S ₁	$^7F_5 \rightarrow ^5I_5$	799	0	0	5.997×10^6	5.997×10^6	1.299×10^5
Total							4.346×10^9	5.562×10^8
6	T ₁	$^7F_6 \rightarrow ^5D_4$	3184	2.201×10^{-1}	2.796×10^2	0	2.799×10^2	9.438×10^{-5}
8	T ₁	$^7F_6 \rightarrow ^5G_6$	-2795	2.355×10^{-5}	8.331×10^{-4}	1.865×10^3	1.865×10^3	1.236×10^9
45	T ₁	$^7F_5 \rightarrow ^5D_4$	5232	2.825×10^{-1}	2.468×10^3	5.765×10^7	5.765×10^7	8.293×10^{-4}
47	T ₁	$^7F_5 \rightarrow ^5G_6$	-747	6.691×10^{-2}	6.183×10^1	7.307×10^6	7.307×10^6	2.224×10^{-8}
49	T ₁	$^7F_5 \rightarrow ^5G_5$	-2091	5.277×10^{-5}	2.087×10^{-3}	3.277×10^4	3.277×10^4	7.426×10^8
Total							6.499×10^7	2.529×10^9

Table S9. Energy transfer rates (in s^{-1}) for **2** considering the ligand-to-Eu^{III} process. δ is the donor-acceptor (singlet/triplet-Eu^{III}) energy difference (in cm^{-1}). We summarize in this table only the pathways contributing more than 0.001% of the total 40 pathways (1–40). W_{d-d} , W_{m-d} , W_{ex} are the dipole-dipole, dipole-multipole, and exchange rates, respectively. W and W^b are the total forward and backward energy transfer rates (sum of each component), respectively at 300.15 K. **2** = [Ln(tfa)₃(μ-dppbo)]_n (Ln = Eu, Tb).

Pathway	Donor	Acceptor	δ	W_{d-d}	W_{m-d}	W_{ex}	W	W_b
7	S ₁	⁷ F ₀ → ⁵ D ₁	17610	0	0	8.953×10 ⁻²	8.953×10 ⁻²	7.513×10 ⁻³⁹
10	S ₁	⁷ F ₀ → ⁵ L ₆	11312	3.836×10 ¹	2.689×10 ⁰	0	4.105×10 ¹	1.043×10 ⁻²³
15	S ₁	⁷ F ₀ → ⁵ G ₆	9885	9.532×10 ¹	6.680×10 ⁰	0	1.020×10 ²	2.430×10 ⁻²⁰
18	S ₁	⁷ F ₀ → ⁵ D ₄	9051	4.659×10 ¹	7.314×10 ²	0	7.780×10 ²	1.461×10 ⁻¹⁷
26	S ₁	⁷ F ₁ → ⁵ D ₀	19716	0	0	6.062×10 ⁻⁵	6.062×10 ⁻⁵	9.316×10 ⁻⁴⁵
27	S ₁	⁷ F ₁ → ⁵ D ₁	17982	4.738×10 ⁻²	4.274×10 ⁻⁴	2.236×10 ⁻⁶	4.296×10 ⁻⁴	8.999×10 ⁻⁴¹
28	S ₁	⁷ F ₁ → ⁵ D ₂	15526	0	0	2.062×10 ⁻¹	2.062×10 ⁻¹	3.381×10 ⁻³³
29	S ₁	⁷ F ₁ → ⁵ D ₃	12654	8.504×10 ⁻³	1.983×10 ¹	0	1.984×10 ¹	2.229×10 ⁻²⁵
30	S ₁	⁷ F ₁ → ⁵ L ₆	11684	7.944×10 ⁻¹	5.568×10 ⁻²	0	8.501×10 ⁻¹	5.389×10 ⁻²⁵
31	S ₁	⁷ F ₁ → ⁵ L ₇	10652	9.326×10 ⁰	6.536×10 ⁻¹	0	9.980×10 ⁰	7.736×10 ⁻²²
32	S ₁	⁷ F ₁ → ⁵ G ₂	10617	0	0	1.130×10 ⁴	1.130×10 ⁴	3.109×10 ⁻¹⁸
33	S ₁	⁷ F ₁ → ⁵ G ₃	10387	4.689×10 ⁻¹	5.576×10 ⁻²	0	5.581×10 ²	3.304×10 ⁻¹⁹
35	S ₁	⁷ F ₁ → ⁵ G ₅	10257	4.769×10 ⁰	3.343×10 ⁻¹	0	5.104×10 ⁰	3.035×10 ⁻²¹
36	S ₁	⁷ F ₁ → ⁵ G ₆	10246	9.800×10 ⁰	3.703×10 ⁰	0	1.350×10 ¹	1.000×10 ⁻²⁰
Total							1.283×10 ⁴	1.809×10 ⁻¹⁷
7	T ₁	⁷ F ₀ → ⁵ D ₁	4428	0	0	3.863×10 ⁸	3.863×10 ⁸	9.265×10 ⁻²
26	T ₁	⁷ F ₁ → ⁵ D ₀	6534	0	0	4.097×10 ⁷	4.097×10 ⁷	1.800×10 ⁻⁵
27	T ₁	⁷ F ₁ → ⁵ D ₁	4800	3.826×10 ⁻³	3.805×10 ²	2.306×10 ⁴	2.344×10 ⁴	1.403×10 ⁻⁵
28	T ₁	⁷ F ₁ → ⁵ D ₂	2344	0	0	8.037×10 ⁶	8.037×10 ⁶	3.766×10 ²
32	T ₁	⁷ F ₁ → ⁵ G ₂	-2565	0	0	9.739×10 ¹	9.739×10 ¹	7.655×10 ⁷
Total							4.353×10 ⁸	7.656×10 ⁷

Table S10. Energy transfer rates (in s^{-1}) for **2** considering the ligand-to-Tb^{III} process. δ is the donor-acceptor (singlet/triplet-Eu^{III}) energy difference (in cm^{-1}). We summarize in this table only the pathways contributing more than 0.001% of the total 78 pathways (1–78). W_{d-d} , W_{m-d} , W_{ex} are the dipole-dipole, dipole-multipole, and exchange rates, respectively. W and W^b are the total forward and backward energy transfer rates (sum of each component), respectively at 300.15 K. **2** = [Ln(tfa)₃(μ-dppbo)]_n (Ln = Eu, Tb).

Pathway	Donor	Acceptor	δ	W_{d-d}	W_{m-d}	W_{ex}	W	W_b
8	S ₁	⁷ F ₆ → ⁵ G ₆	10214	9.902×10 ¹	7.551×10 ³	1.435×10 ⁶	1.442×10 ⁶	7.671×10 ⁻¹⁶
10	S ₁	⁷ F ₆ → ⁵ G ₅	8870	8.494×10 ¹	1.204×10 ¹	7.100×10 ⁵	7.508×10 ⁵	2.973×10 ⁻¹³
12	S ₁	⁷ F ₆ → ⁵ G ₄	8350	1.052×10 ²	6.785×10 ³	0	6.891×10 ³	4.039×10 ⁻¹⁴
16	S ₁	⁷ F ₆ → ⁵ L ₇	7180	5.935×10 ²	1.642×10 ⁵	5.870×10 ¹	1.648×10 ⁵	1.585×10 ⁻¹⁰
18	S ₁	⁷ F ₆ → ⁵ L ₆	6967	0	0	1.699×10 ⁶	1.699×10 ⁶	5.236×10 ⁻⁹
21	S ₁	⁷ F ₆ → ⁵ H ₇	5258	0	0	9.469×10 ⁶	9.469×10 ⁶	9.174×10 ⁻⁵
22	S ₁	⁷ F ₆ → ⁵ H ₆	3746	0	0	2.179×10 ⁸	2.179×10 ⁸	3.435×10 ⁰
25	S ₁	⁷ F ₆ → ⁵ F ₅	1703	0	0	1.053×10 ⁹	1.053×10 ⁹	3.530×10 ⁵
30	S ₁	⁷ F ₆ → ⁵ I ₇	48	0	0	5.823×10 ⁷	5.823×10 ⁷	4.009×10 ⁷
33	S ₁	⁷ F ₆ → ⁵ I ₆	-961	0	0	7.847×10 ⁶	7.847×10 ⁶	7.876×10 ⁸
35	S ₁	⁷ F ₆ → ⁵ I ₅	-1349	0	0	9.596×10 ⁴	9.596×10 ⁴	7.318×10 ⁷
47	S ₁	⁷ F ₅ → ⁵ G ₆	12262	3.120×10 ⁻¹	6.415×10 ²	6.428×10 ³	7.070×10 ³	1.726×10 ⁻²²
49	S ₁	⁷ F ₅ → ⁵ G ₅	10918	2.078×10 ⁰	1.772×10 ²	2.360×10 ⁵	2.360×10 ⁵	4.294×10 ⁻¹⁸
51	S ₁	⁷ F ₅ → ⁵ G ₄	10398	1.569×10 ⁰	2.072×10 ³	7.025×10 ⁴	7.233×10 ⁴	1.946×10 ⁻¹⁷
55	S ₁	⁷ F ₅ → ⁵ L ₇	9228	2.928×10 ¹	4.872×10 ³	0	4.901×10 ³	2.163×10 ⁻¹⁶
57	S ₁	⁷ F ₅ → ⁵ L ₆	9015	0	0	2.200×10 ⁴	2.200×10 ⁴	3.112×10 ⁻¹⁵
61	S ₁	⁷ F ₅ → ⁵ H ₆	5794	0	0	7.389×10 ⁶	7.389×10 ⁶	5.346×10 ⁻⁶
62	S ₁	⁷ F ₅ → ⁵ H ₅	4918	0	0	1.903×10 ⁸	1.903×10 ⁸	1.086×10 ⁻²
63	S ₁	⁷ F ₅ → ⁵ H ₄	4346	0	0	6.538×10 ⁸	6.538×10 ⁸	7.088×10 ⁻¹
64	S ₁	⁷ F ₅ → ⁵ F ₅	3751	0	0	5.487×10 ⁸	5.487×10 ⁸	8.445×10 ⁰
67	S ₁	⁷ F ₅ → ⁵ F ₄	3311	0	0	2.107×10 ⁹	2.107×10 ⁹	3.270×10 ²
72	S ₁	⁷ F ₅ → ⁵ I ₆	1087	0	0	1.369×10 ⁸	1.369×10 ⁸	6.305×10 ⁵
74	S ₁	⁷ F ₅ → ⁵ I ₅	699	0	0	9.897×10 ⁶	9.897×10 ⁶	3.464×10 ⁵
75	S ₁	⁷ F ₅ → ⁵ K ₅	-2649	0	0	5.088×10 ⁰	5.088×10 ⁰	1.675×10 ⁶
Total							5.005×10 ⁹	9.046×10 ⁸
6	T ₁	⁷ F ₆ → ⁵ D ₄	3011	1.013×10 ⁻¹	3.229×10 ²	0	3.230×10 ²	2.497×10 ⁻⁴
8	T ₁	⁷ F ₆ → ⁵ G ₆	-2968	1.013×10 ⁻⁶	3.869×10 ⁻⁴	8.526×10 ²	8.526×10 ²	1.296×10 ⁹
45	T ₁	⁷ F ₅ → ⁵ D ₄	5059	6.816×10 ⁻²	1.684×10 ³	3.872×10 ⁷	3.872×10 ⁷	1.374×10 ⁻³
47	T ₁	⁷ F ₅ → ⁵ G ₆	-920	1.704×10 ⁻⁴	3.873×10 ¹	4.505×10 ⁶	4.505×10 ⁶	3.143×10 ⁸
49	T ₁	⁷ F ₅ → ⁵ G ₅	-2264	1.176×10 ⁻⁵	1.109×10 ⁻³	1.714×10 ⁴	1.714×10 ⁴	8.906×10 ⁸
Total							4.324×10 ⁷	2.680×10 ⁹

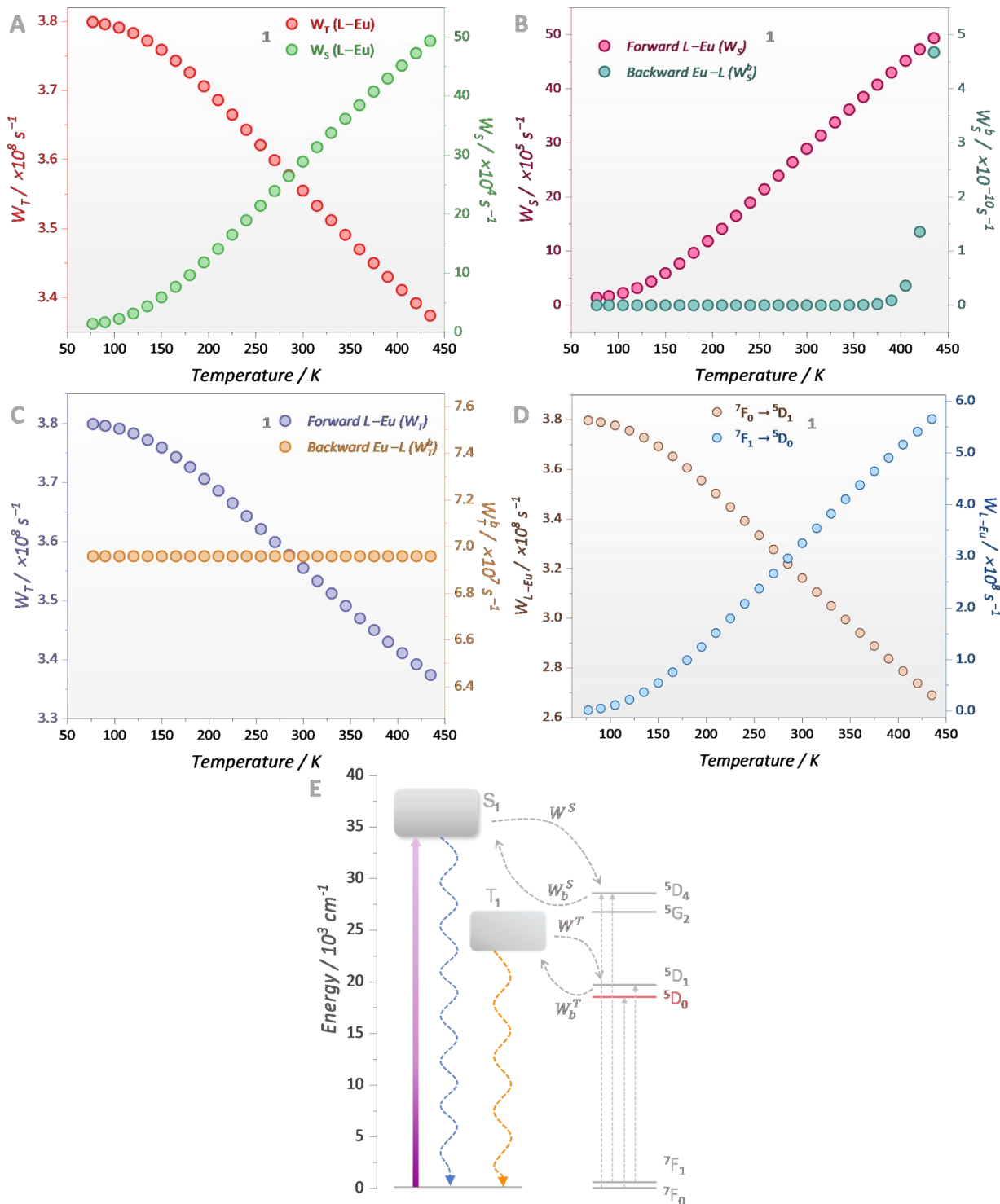


Fig S12. Temperature dependent IET ligand-to-Eu^{III} rates for coordination polymer **1** focusing on (a) energy transfer arising from the singlet and triplet state to Eu^{III}; (b) the forward and backward energy transfer rates (Eu^{III}-Ligand) from the singlet state and (c) from the triplet state; (d) temperature dependence of the energy transfer from the triplet state concerning the ${}^7\text{F}_0$ and ${}^7\text{F}_1$ manifold; (e) Partial energy transfer diagram highlighting the process described in Fig. S13 a,b,c,d. **1** = [Ln(tfa)₃(μ-dppeo)]_n (Ln = Eu, Tb).

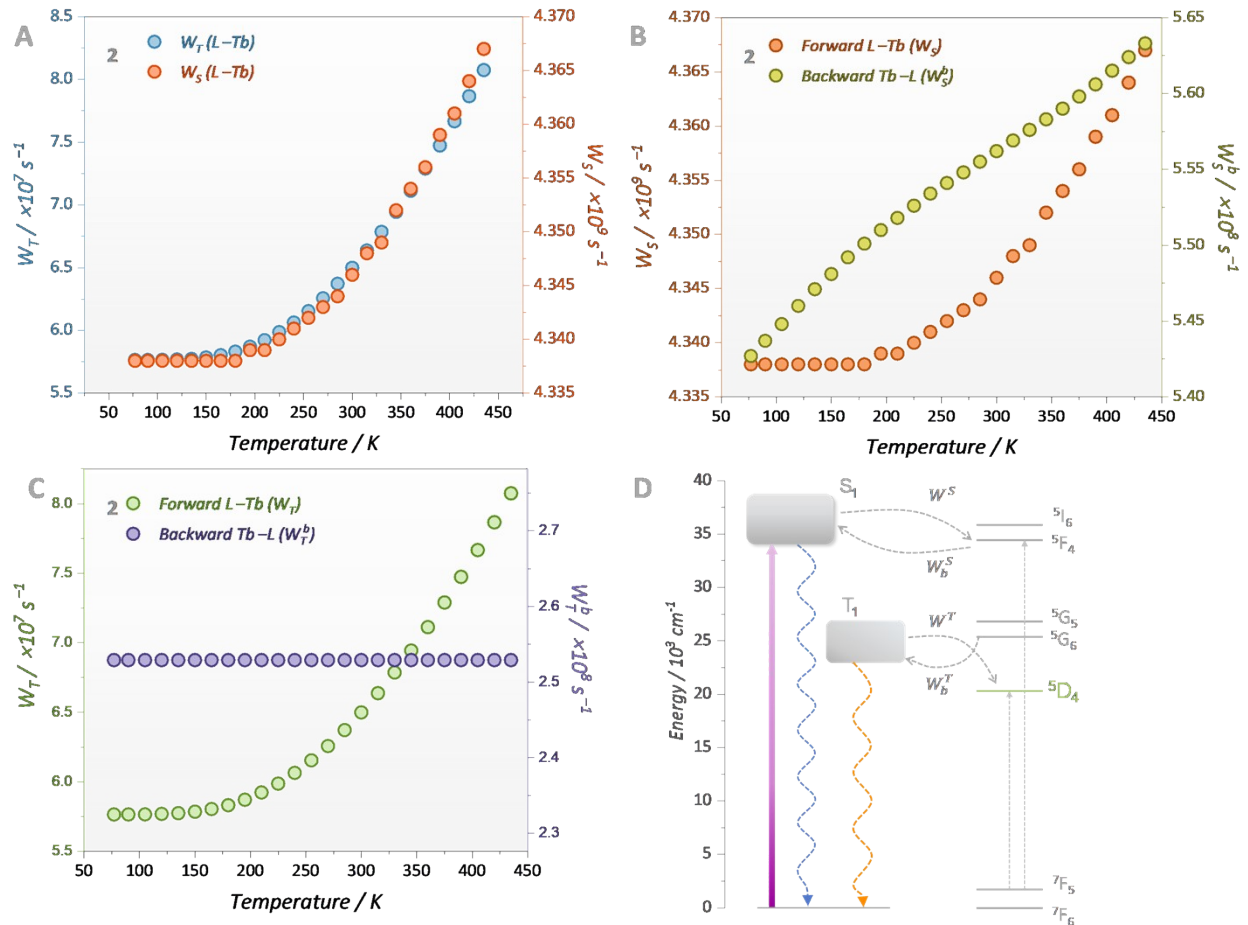


Fig S13. Temperature dependent IET ligand-to-Tb^{III} rates for coordination polymer **1** focusing on (a) energy transfer arising from the singlet and triplet state to Eu^{III}; (b) the forward and backward energy transfer rates from the singlet state and (c) from the triplet state; (d) Partial energy transfer diagram highlighting the process described in Fig. S10 a,b,c. **1** = $[\text{Ln}(\text{tfa})_3(\mu\text{-dppeo})]_n$ (Ln = Eu, Tb).

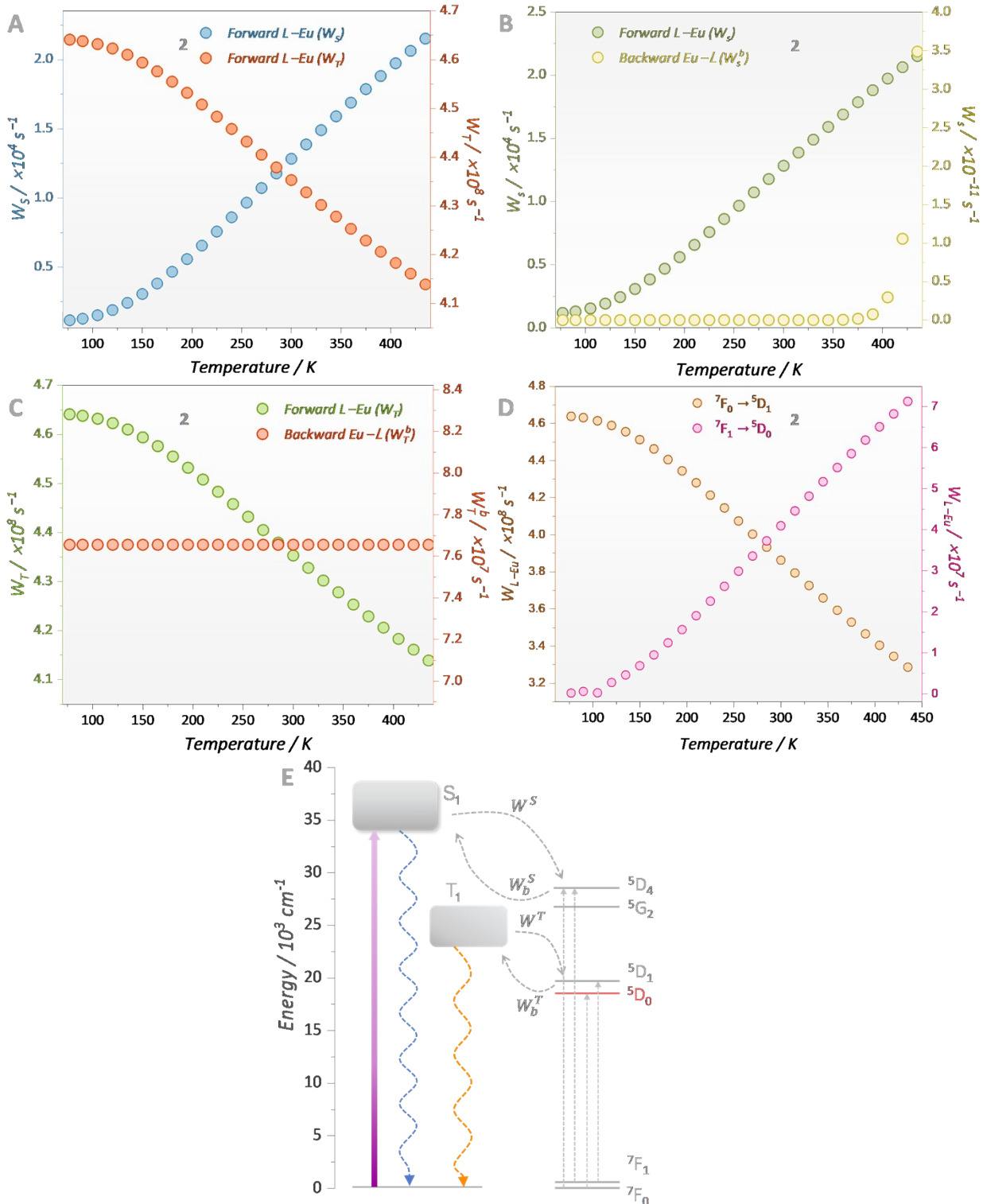


Fig S14. Temperature dependent IET ligand-to-Eu^{III} rates for coordination polymer **2** focusing on (a) energy transfer arising from the singlet and triplet state to Eu^{III}; (b) the forward and backward energy transfer rates from the singlet state and (c) from the triplet state; (d) Partial energy transfer diagram highlighting the process described in Fig. S11 a,b,c,d. **2** = [Ln(tfa)₃(μ-dppbo)]_n (Ln = Eu, Tb).

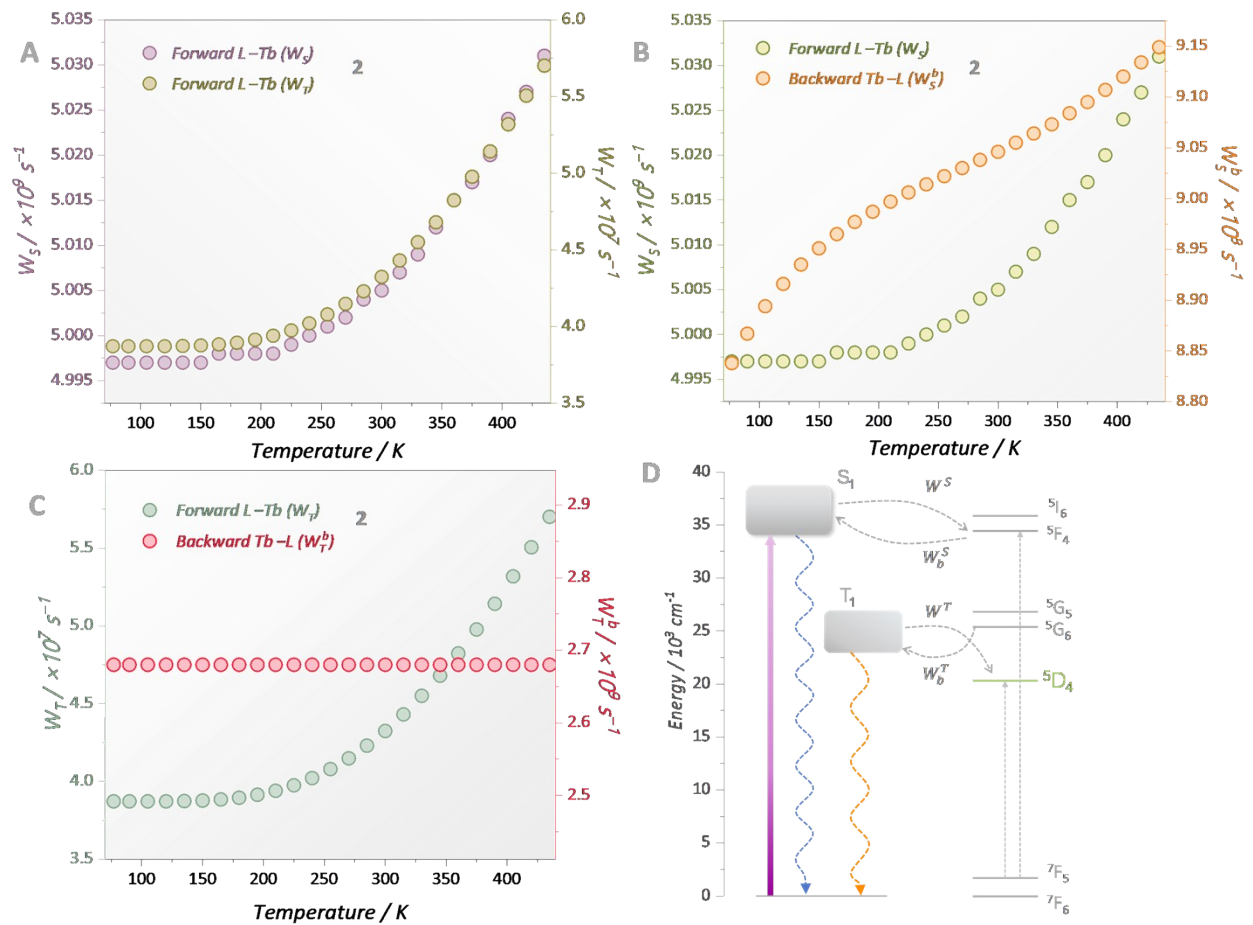


Fig S15. Temperature dependent IET ligand-to-Tb^{III} rates for coordination polymer **2** focusing on (a) energy transfer arising from the singlet and triplet state to Eu^{III}; (b) the forward and backward energy transfer rates from the singlet state and (c) from the triplet state; (d) Partial energy transfer diagram highlighting the process described in Fig. S12 a,b,c,d. **2** = [Ln(tfa)₃(μ-dppbo)]_n (Ln = Eu, Tb).

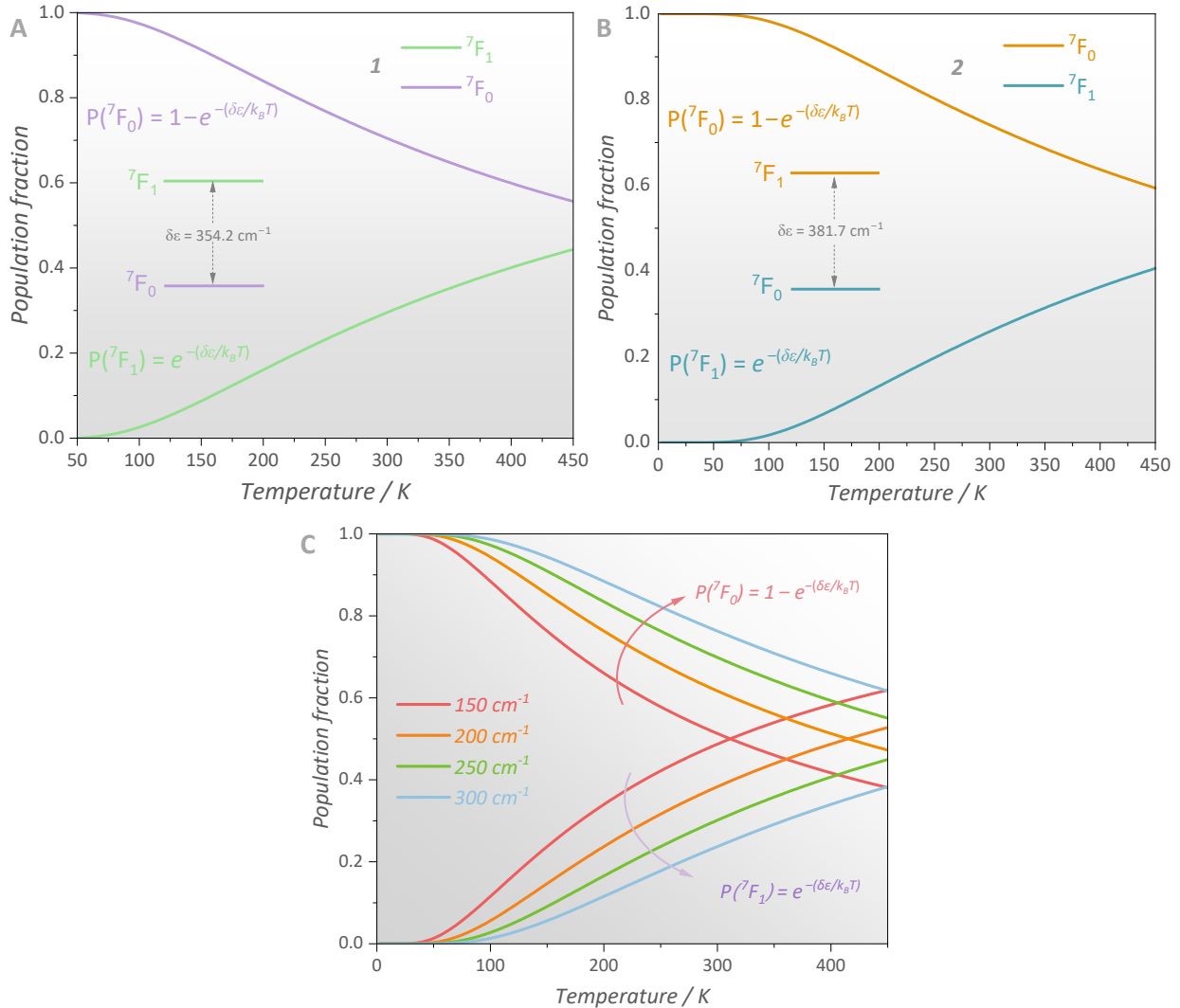


Fig S16. Thermal population of the 7F_0 and 7F_1 manifolds for (a) **1** and (b) **2**. The energy difference between the two levels ($\delta\varepsilon$) was obtained by the difference of the emission band's barycenter in the experimental spectra. (c) Trend in the thermal population of 7F_1 level for various energies difference. **1** = $[\text{Ln(tfa)}_3(\mu\text{-dppeo})]_n$; **2** = $[\text{Ln(tfa)}_3(\mu\text{-dppbo})]_n$ ($\text{Ln} = \text{Eu, Tb}$).

Supplementary note S7 – Multiphonon relaxation

Among the relaxation pathways that can occur in a Ln^{III} -based compound, the non-radiative decay is often associated with the multiphonon relaxation, i.e, the sequential absorption and emission of a phonon to bridge the energy gap between two electronic states (Fig S17 for the Eu^{III} part).

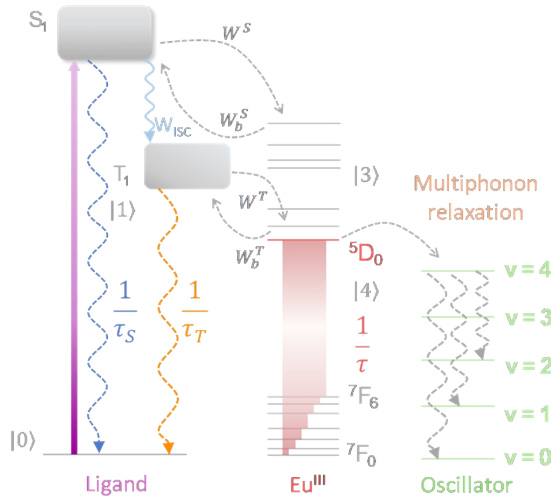


Fig S17. Representation of the multiphonon relaxation for the Eu^{III} counterpart.

For the determination of the multiphonon relaxation rates by the Miyakawa-Dexter model³⁴, the mean phonon energy is needed. Instead of using the energy of the maximum vibrational normal mode, previous studies on thermally activated delayed fluorescent materials shows that all normal modes do not contribute the same to the mean phonon energy^{43,44}. Therefore, we employed the weighted energy by the vibrational intensity (Fig S18).

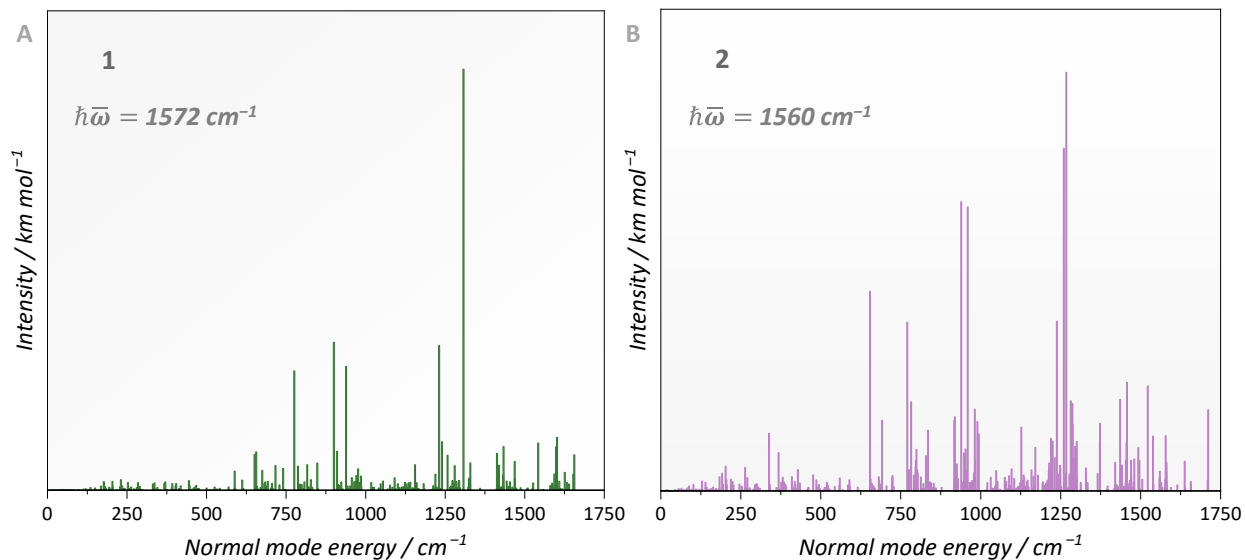


Fig S18. Normal mode energies highlight the mean phonon energy weighted by its intensity for (a) **1** and (b) **2**. **1** = $[\text{Ln}(\text{tfa})_3(\mu\text{-dppeo})]_n$; **2** = $[\text{Ln}(\text{tfa})_3(\mu\text{-dppbo})]_n$ ($\text{Ln} = \text{Eu}, \text{Tb}$).

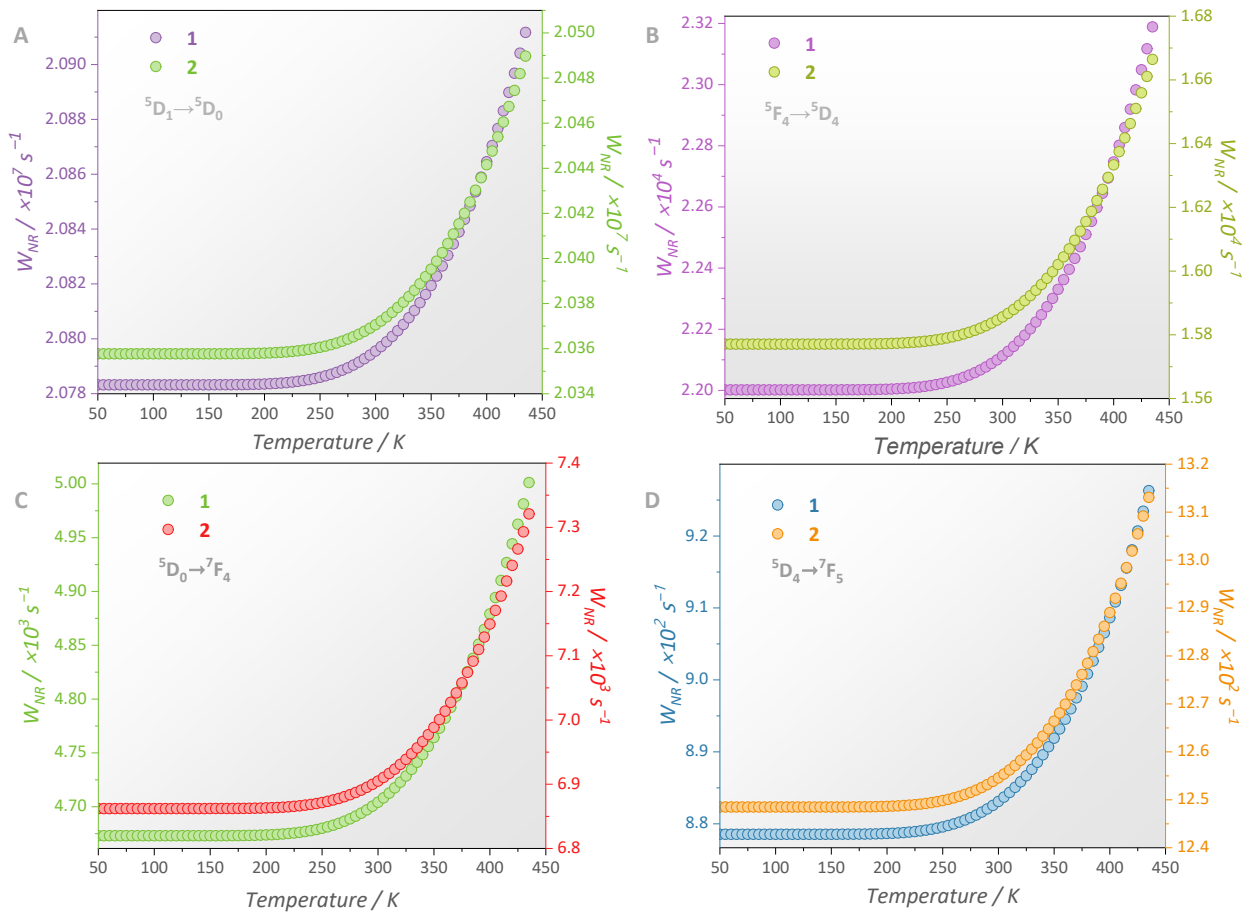


Fig S19. Rates of multiphonon relaxation for **1** and **2** considering the Huang-Rhys factor of 0.1. The decay from upper emitting levels to the ${}^5\text{D}_0$ and ${}^5\text{D}_4$ of Eu^{III} and Tb^{III}, respectively are represented in item (a) and (b), respectively. The multiphonon decay rates considering the relaxation from the emitting level to the ground state are displayed in item (c) for Eu^{III} (${}^5\text{D}_0 \rightarrow {}^7\text{F}_4$) and (d) for Tb^{III} (${}^5\text{D}_4 \rightarrow {}^7\text{F}_5$). **1** = [Ln(tfa)₃(μ-dppeo)]_n; **2** = [Ln(tfa)₃(μ-dppbo)]_n (Ln = Eu, Tb).

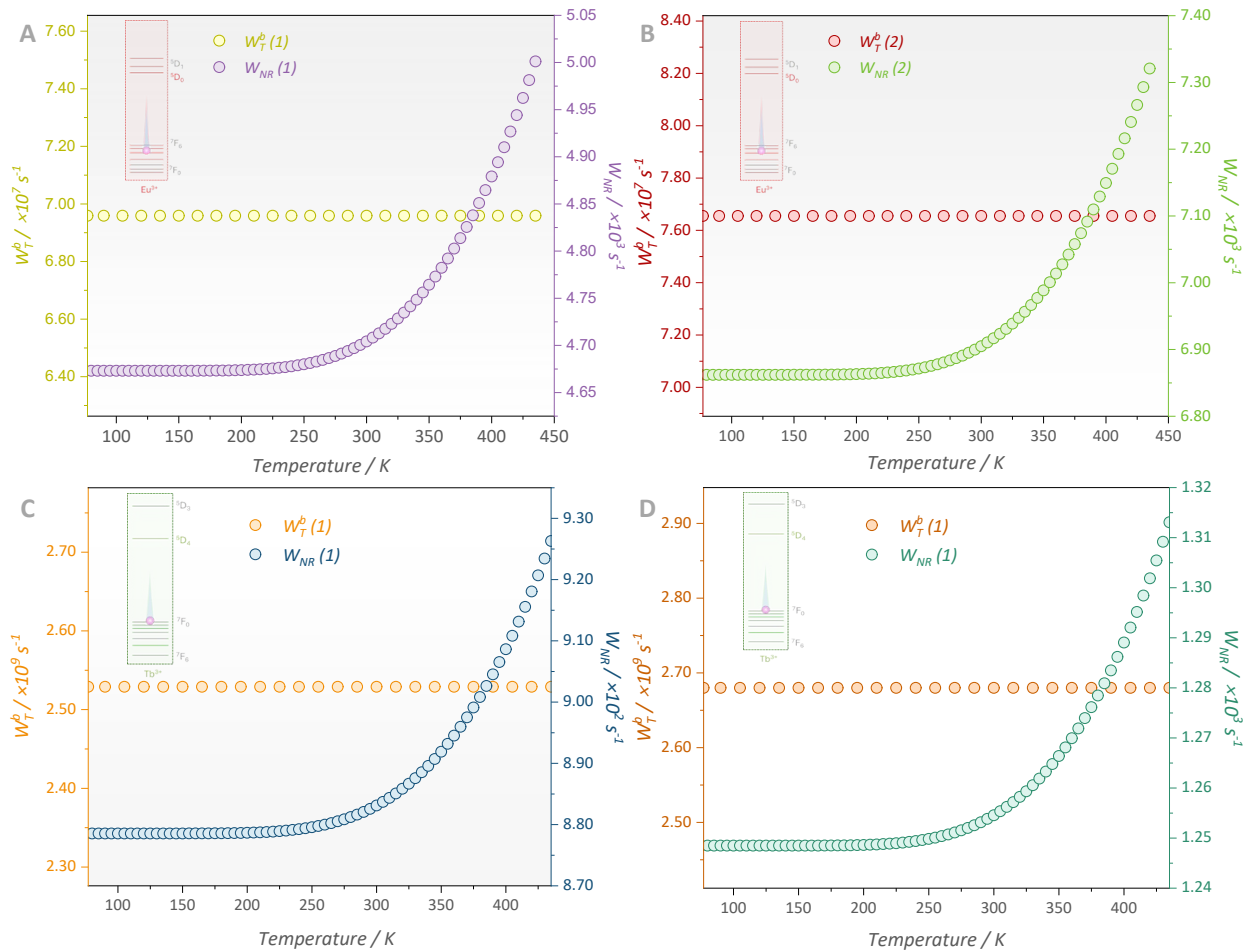


Fig S20. Comparison of Ligand-to-Ln^{III} backward ET and multiphonon relaxation dependence with temperature regarding the excited state. Considering Eu³⁺ for (a) **1** and (b) **2**, and Tb³⁺ for (c) **1** and (d) **2**. **1** = [Ln(tfa)₃(μ-dppeo)]_n; **2** = [Ln(tfa)₃(μ-dppbo)]_n (Ln = Eu, Tb).

Supplementary note S8 – Ln^{III}-to-Ln^{III} energy transfer

Analogous to the case of ligand-to-Ln^{III} energy transfer, the Ln^{III}-to-Ln^{III} process is pivotal when considering all photophysical phenomenon occurring in the coordination compound. For this reason, we determined the rates of ET between Eu^{III} and Tb^{III} varying the distance between both centers considering the Tb^{III} 4f excitation. The calculations were performed for all inter- and intramolecular distances between both ions (Fig 2), however, for sake of clarity we will only highlight the table for one of the intramolecular distances for complexes **1** and **2**, since the process is the same for each calculation. We emphasize that the population of the acceptor ground-state needs to be considered in the determination, therefore, this factor is represented in Fig S16. To ensure that only these distances need consideration, a 3x3x3 supercell of **1** and **2** are represented in Fig. S22, demonstrating that the structures are ordered. Hence, precluding the necessity to simulate multiple distances. It is noteworthy that all energy transfer rates for each distance as a function of temperature are highlighted directly in Fig. S23.

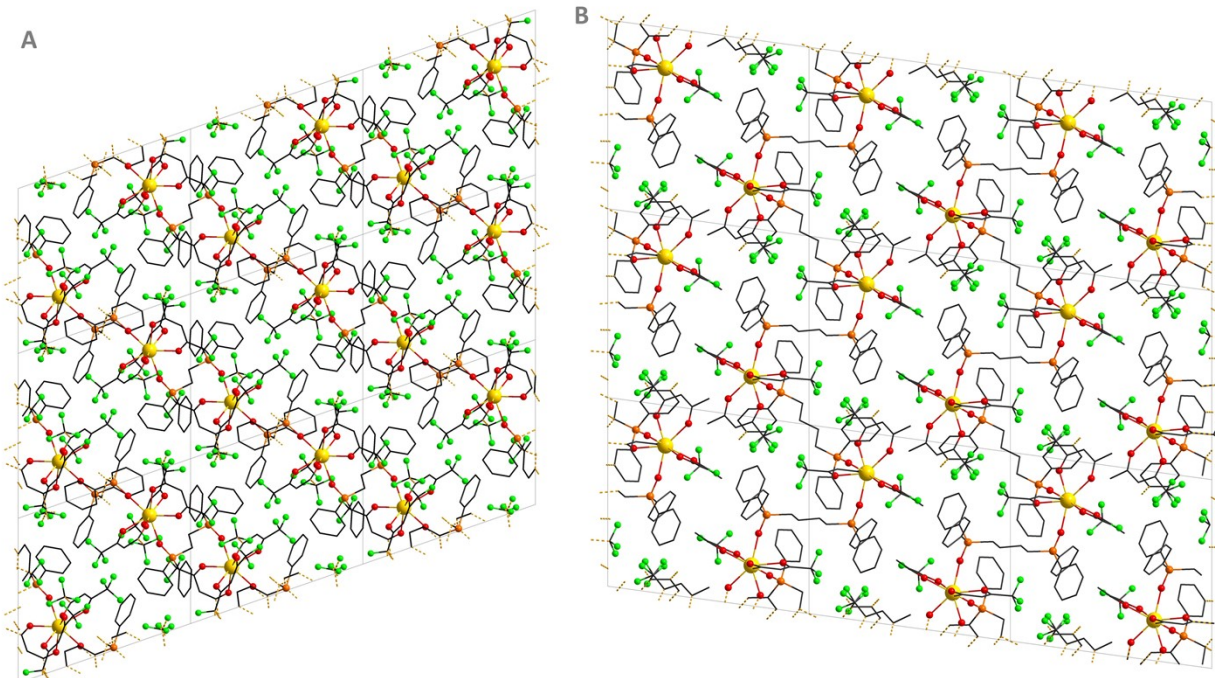


Figure S21. Packing diagram of (a) **1** and (b) **2**. Representation along the α axis. H atoms have been omitted for the sake of clarity. **1** = [Ln(tfa)₃(μ -dppeo)]_n; **2** = [Ln(tfa)₃(μ -dppbo)]_n (Ln = Eu, Tb).

Table S11. Tb^{III}-to-Eu^{III} energy transfer rates at 300 K considering the intramolecular distance ($R_{Tb-Eu} = 8.298 \text{ \AA}$) for **1**. W_{d-d} , W_{d-q} , W_{q-q} , W_{ex} , and W_{md-md} are the dipole-dipole, dipole-quadrupole, quadrupole-quadrupole, exchange, and magnetic dipole-magnetic dipole mechanisms in s^{-1} , respectively. W is the sum of each pathway and the $W_{Tb \rightarrow Eu}$ is the sum of all pathways. δ is the energy difference (in cm^{-1}) between donor and acceptor states. **1** = [Ln(tfa)₃(μ-dppeo)]_n (Ln = Eu, Tb).

Path	Donor	Accepto r	δ	W_{d-d}	W_{d-q}	W_{q-q}	W_{ex}	W_{md-md}	W
1	⁵ D ₄ → ⁷ F ₆	⁷ F ₀ → ⁵ D ₀	3151	5.212 × 10 ⁻¹⁹	5.368 × 10 ⁻¹⁵	5.918 × 10 ⁻¹²	2.066 × 10 ⁻⁴³	0	4.144 × 10 ⁻¹¹
2	⁵ D ₄ → ⁷ F ₆	⁷ F ₀ → ⁵ D ₁	1417	0	0	0	1.116 × 10 ⁻³³	0	7.810 × 10 ⁻³³
3	⁵ D ₄ → ⁷ F ₆	⁷ F ₀ → ⁵ D ₂	-1039	0	0	0	1.06 × 10 ⁻³⁴	0	7.417 × 10 ⁻³⁴
4	⁵ D ₄ → ⁷ F ₆	⁷ F ₁ → ⁵ D ₀	3523	0	0	0	2.890 × 10 ⁻⁴⁵	0	8.669 × 10 ⁻⁴⁵
5	⁵ D ₄ → ⁷ F ₆	⁷ F ₁ → ⁵ D ₁	1789	2.510 × 10 ⁻¹¹	2.585 × 10 ⁻⁷	2.850 × 10 ⁻⁴	3.820 × 10 ⁻³⁵	0	8.557 × 10 ⁻⁵
6	⁵ D ₄ → ⁷ F ₆	⁷ F ₁ → ⁵ D ₂	-667	0	0	0	3.790 × 10 ⁻³³	0	1.137 × 10 ⁻³³
7	⁵ D ₄ → ⁷ F ₅	⁷ F ₀ → ⁵ D ₀	1103	2.016 × 10 ⁻⁸	2.254 × 10 ⁻⁴	1.577 × 10 ⁰	1.046 × 10 ⁻³²	0	4.730 × 10 ⁰
8	⁵ D ₄ → ⁷ F ₅	⁷ F ₀ → ⁵ D ₁	-631	0	0	0	5.141 × 10 ⁻³³	3.323 × 10 ⁻³	2.326 × 10 ⁻³
9	⁵ D ₄ → ⁷ F ₅	⁷ F ₀ → ⁵ D ₂	-3087	0	0	0	2.394 × 10 ⁻⁴⁹	0	1.676 × 10 ⁻⁴⁸
10	⁵ D ₄ → ⁷ F ₅	⁷ F ₁ → ⁵ D ₀	1475	0	0	0	6.940 × 10 ⁻³⁴	6.398 × 10 ⁻⁴	1.919 × 10 ⁻⁴
11	⁵ D ₄ → ⁷ F ₅	⁷ F ₁ → ⁵ D ₁	-259	1.175 × 10 ⁻⁷	1.314 × 10 ⁻³	9.193 × 10 ¹	7.811 × 10 ⁻³²	5.539 × 10 ⁻⁴	3.758 × 10 ¹
12	⁵ D ₄ → ⁷ F ₅	⁷ F ₁ → ⁵ D ₂	-2715	0	0	0	6.348 × 10 ⁻⁴⁶	2.301 × 10 ⁻¹⁷	6.903 × 10 ⁻¹⁸
13	⁵ D ₄ → ⁷ F ₄	⁷ F ₀ → ⁵ D ₀	-164	5.099 × 10 ⁻⁷	5.187 × 10 ⁻³	8.790 × 10 ⁻¹	1.380 × 10 ⁻³¹	0	6.190 × 10 ⁻¹
14	⁵ D ₄ → ⁷ F ₄	⁷ F ₀ → ⁵ D ₁	-1898	0	0	0	1.365 × 10 ⁻³⁹	3.375 × 10 ⁻¹⁰	2.362 × 10 ⁻¹⁰
15	⁵ D ₄ → ⁷ F ₄	⁷ F ₀ → ⁵ D ₂	-4354	0	0	0	1.423 × 10 ⁻⁶³	0	9.959 × 10 ⁻⁶⁴
16	⁵ D ₄ → ⁷ F ₄	⁷ F ₁ → ⁵ D ₀	208	0	0	0	2.893 × 10 ⁻³¹	1.020 × 10 ⁻¹	3.100 × 10 ⁻²
17	⁵ D ₄ → ⁷ F ₄	⁷ F ₁ → ⁵ D ₁	-1667	2.872 × 10 ⁻¹³	2.921 × 10 ⁻⁹	4.948 × 10 ⁻⁷	2.985 × 10 ⁻³⁷	8.110 × 10 ⁻¹⁰	1.496 × 10 ⁻⁷
18	⁵ D ₄ → ⁷ F ₄	⁷ F ₁ → ⁵ D ₂	-4123	0	0	0	5.472 × 10 ⁻⁵⁹	7.599 × 10 ⁻³¹	2.280 × 10 ⁻³¹
19	⁵ D ₄ → ⁷ F ₃	⁷ F ₀ → ⁵ D ₀	-1143	4.750 × 10 ⁻¹¹	5.116 × 10 ⁻⁷	2.236 × 10 ⁻³	3.193 × 10 ⁻³⁵	0	1.565 × 10 ⁻³
20	⁵ D ₄ → ⁷ F ₃	⁷ F ₀ → ⁵ D ₁	-2877	0	0	0	2.025 × 10 ⁻⁴⁷	5.519 × 10 ⁻²⁷	3.864 × 10 ⁻²⁷
21	⁵ D ₄ → ⁷ F ₃	⁷ F ₀ → ⁵ D ₂	-5333	0	0	0	2.430 × 10 ⁻⁷⁷	0	1.701 × 10 ⁻⁷⁷
22	⁵ D ₄ → ⁷ F ₃	⁷ F ₁ → ⁵ D ₀	-912	0	0	0	1.440 × 10 ⁻³³	5.608 × 10 ⁻³	1.682 × 10 ⁻³

23	$^5D_4 \rightarrow ^7F_3$	$^7F_1 \rightarrow ^5D_1$	-2646	1.361×10^{-20}	1.466×10^{-16}	6.407×10^{-13}	3.513×10^{-44}	1.052×10^{-15}	1.926×10^{-13}
24	$^5D_4 \rightarrow ^7F_3$	$^7F_1 \rightarrow ^5D_2$	-5102	0	0	0	7.416×10^{-72}	1.135×10^{-43}	3.406×10^{-43}
Total									$W_{Tb \rightarrow Eu}$

Table S12. Tb^{III}-to-Eu^{III} energy transfer rates at 300 K considering the intramolecular distance ($R_{Tb-Eu} = 10.820$ Å) for **2**. W_{d-d} , W_{d-q} , W_{q-q} , W_{ex} , and W_{md-md} are the dipole-dipole, dipole-quadrupole, quadrupole-quadrupole, exchange, and magnetic dipole-magnetic dipole mechanisms (in s⁻¹), respectively. W is the sum of each pathway and the $W_{Tb \rightarrow Eu}$ is the sum of all pathways. δ is the energy difference (in cm⁻¹) between donor and acceptor states. **2** = [Ln(tfa)₃(μ-dppbo)]_n (Ln = Eu, Tb).

Pat h	Donor	Accepto r	δ	W_{d-d}	W_{d-q}	W_{q-q}	W_{ex}	W_{md-md}	W
1	$^5D_4 \rightarrow ^7F_6$	$^7F_0 \rightarrow ^5D_0$	3151	4.607×10^{-20}	3.228×10^{-16}	4.165×10^{-13}	4.672×10^{-75}	0	2.751×10^{-13}
2	$^5D_4 \rightarrow ^7F_6$	$^7F_0 \rightarrow ^5D_1$	1417	0	0	0	2.523×10^{-65}	0	1.665×10^{-65}
3	$^5D_4 \rightarrow ^7F_6$	$^7F_0 \rightarrow ^5D_2$	-1039	0	0	0	2.390×10^{-66}	0	1.578×10^{-66}
4	$^5D_4 \rightarrow ^7F_6$	$^7F_1 \rightarrow ^5D_0$	3523	0	0	0	4.159×10^{-78}	0	2.745×10^{-78}
5	$^5D_4 \rightarrow ^7F_6$	$^7F_1 \rightarrow ^5D_1$	1789	2.219×10^{-12}	1.555×10^{-8}	2.006×10^{-5}	8.639×10^{-67}	0	6.624×10^{-6}
6	$^5D_4 \rightarrow ^7F_6$	$^7F_1 \rightarrow ^5D_2$	-667	0	0	0	8.572×10^{-65}	0	2.829×10^{-65}
7	$^5D_4 \rightarrow ^7F_5$	$^7F_0 \rightarrow ^5D_0$	1103	5.337×10^{-9}	4.298×10^{-5}	2.330×10^{-1}	2.366×10^{-64}	0	1.200×10^0
8	$^5D_4 \rightarrow ^7F_5$	$^7F_0 \rightarrow ^5D_1$	-631	0	0	0	1.163×10^{-64}	6.750×10^{-4}	4.455×10^{-4}
9	$^5D_4 \rightarrow ^7F_5$	$^7F_0 \rightarrow ^5D_2$	-3087	0	0	0	≈ 0	0	≈ 0
10	$^5D_4 \rightarrow ^7F_5$	$^7F_1 \rightarrow ^5D_0$	1475	0	0	0	1.570×10^{-65}	1.302×10^{-4}	4.296×10^{-5}
11	$^5D_4 \rightarrow ^7F_5$	$^7F_1 \rightarrow ^5D_1$	-259	1.037×10^{-8}	8.355×10^{-5}	6.740×10^{-1}	1.766×10^{-63}	1.127×10^{-4}	2.140×10^0
12	$^5D_4 \rightarrow ^7F_5$	$^7F_1 \rightarrow ^5D_2$	-2715	0	0	0	1.436×10^{-77}	4.681×10^{-18}	1.545×10^{-18}
13	$^5D_4 \rightarrow ^7F_4$	$^7F_0 \rightarrow ^5D_0$	-164	4.360×10^{-8}	2.990×10^{-4}	6.200×10^{-2}	3.122×10^{-63}	0	4.100×10^{-1}
14	$^5D_4 \rightarrow ^7F_4$	$^7F_0 \rightarrow ^5D_1$	-1898	0	0	0	3.101×10^{-71}	6.898×10^{-11}	4.552×10^{-11}
15	$^5D_4 \rightarrow ^7F_4$	$^7F_0 \rightarrow ^5D_2$	-4354	0	0	0	≈ 0	0	≈ 0
16	$^5D_4 \rightarrow ^7F_4$	$^7F_1 \rightarrow ^5D_0$	208	0	0	0	6.543×10^{-63}	2.100×10^{-2}	6.862×10^{-3}
17	$^5D_4 \rightarrow ^7F_4$	$^7F_1 \rightarrow ^5D_1$	-1526	2.464×10^{-14}	1.690×10^{-10}	3.495×10^{-8}	6.775×10^{-69}	1.656×10^{-10}	1.164×10^{-8}
18	$^5D_4 \rightarrow ^7F_4$	$^7F_1 \rightarrow ^5D_2$	-3982	0	0	0	≈ 0	1.561×10^{-31}	5.151×10^{-32}

19	$^5D_4 \rightarrow ^7F_3$	$^7F_0 \rightarrow ^5D_0$	-1148	4.171×10^{-12}	3.158×10^{-8}	1.578×10^{-4}	7.240×10^{-67}	0	1.042×10^{-3}
20	$^5D_4 \rightarrow ^7F_3$	$^7F_0 \rightarrow ^5D_1$	-2882	0	0	0	4.611×10^{-79}	1.131×10^{-17}	7.463×10^{-18}
21	$^5D_4 \rightarrow ^7F_3$	$^7F_0 \rightarrow ^5D_2$	-5338	0	0	0	≈ 0	0	≈ 0
22	$^5D_4 \rightarrow ^7F_3$	$^7F_1 \rightarrow ^5D_0$	-776	0	0	0	3.263×10^{-65}	1.143×10^{-3}	3.772×10^{-4}
23	$^5D_4 \rightarrow ^7F_3$	$^7F_1 \rightarrow ^5D_1$	-2510	1.199×10^{-21}	9.080×10^{-18}	4.537×10^{-14}	7.993×10^{-76}	2.154×10^{-16}	1.504×10^{-14}
24	$^5D_4 \rightarrow ^7F_3$	$^7F_1 \rightarrow ^5D_2$	-4966	0	0	0	≈ 0	2.338×10^{-43}	7.715×10^{-44}
$W_{Tb \rightarrow Eu}$									0.4369×10^1

Table S13. Total Tb^{III}-Eu^{III} energy transfer rates considering both intra- and intermolecular Tb^{III}-Eu^{III} distances at 300.15 K. **1** = [Ln(tfa)₃(μ-dppeo)]_n; **2** = [Ln(tfa)₃(μ-dppbo)]_n (Ln = Eu, Tb).

	Intramolecular		Intermolecular	
	$R_{Tb-Eu} / \text{\AA}$	$W_{Tb \rightarrow Eu} / \text{s}^{-1}$	$R_{Tb-Eu} / \text{\AA}$	$W_{Tb \rightarrow Eu} / \text{s}^{-1}$
1	8.298	4.883×10^1	11.66	1.696×10^0
	8.559	4.604×10^1	—	—
	10.82	0.4369×10^1	8.114	6.402×10^1
2	11.10	0.1062×10^1	—	—
	13.55	0.1389×10^0	—	—

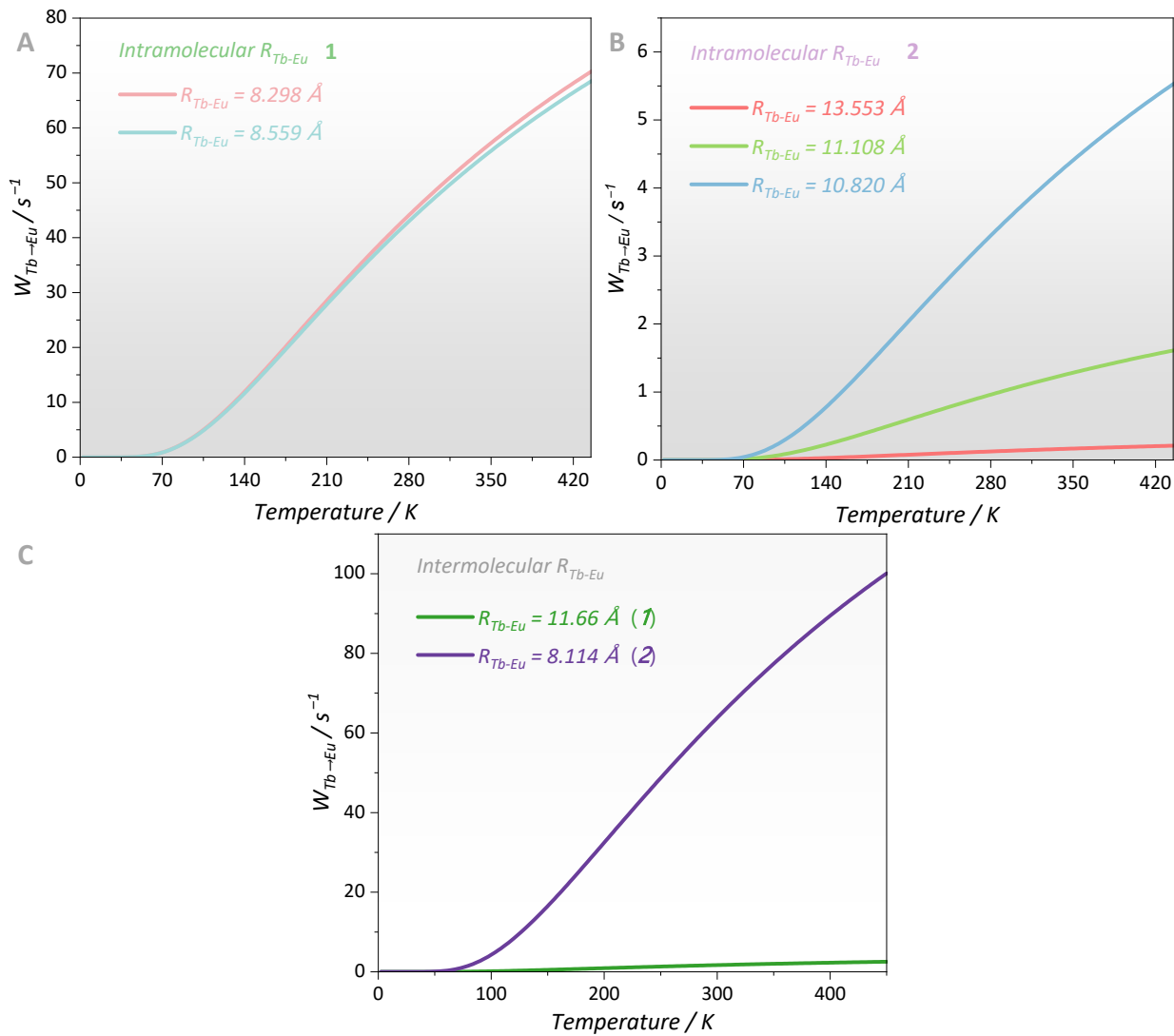


Fig S22. Temperature dependent rates of Tb^{III} -to- Eu^{III} energy transfer for the intramolecular Tb^{III} - Eu^{III} distances in (a) **1** and (b) **2**. The rates of energy transfer considering the intermolecular Tb^{III} - Eu^{III} distances were also determined in (c). For all calculations, the direct Tb^{III} excitation (481 nm) was considered. **1** = $[\text{Ln}(\text{tfa})_3(\mu\text{-dppeo})]_n$; **2** = $[\text{Ln}(\text{tfa})_3(\mu\text{-dppbo})]_n$ ($\text{Ln} = \text{Eu}, \text{Tb}$).

Supplementary note S9 – Population dynamics and theoretical thermometry

With the ligand-to-Ln^{III} intramolecular energy transfer and Ln^{III}-to-Ln^{III} energy transfer rates, as well as with the emission lifetime of both Tb^{III} and Eu^{III}, and the multiphonon decay rates, the next step to accurately describe the photophysical dynamics involves in obtaining the population of each emitting state. To do so, we can construct a set of coupled ordinary differential equations (ODEs), as evinced in Eq. S31. This system can be solved numerically through time propagation, enabling the obtention of the population dynamics of each level. From this perspective, Eq. S40 and S41 were constructed and solved using Radau methods³⁶.

Under ligand excitation (340 nm)

$$|0\rangle: \frac{d}{dt}P_0 = -\phi P_0(t) + \frac{1}{\tau_T}P_1(t) + \frac{1}{\tau_S}P_2(t) + \frac{1}{\tau}P_4(t) \quad (S40a)$$

$$|1\rangle: \frac{d}{dt}P_1 = -\left(\frac{1}{\tau_T} + W^T\right)P_1(t) + W_{ISC}P_2(t) + W_b^TP_3(t) \quad (S40b)$$

$$|2\rangle: \frac{d}{dt}P_2 = -\left(\frac{1}{\tau_S} + W^S + W_{ISC}\right)P_2(t) + W_b^SP_3(t) + \phi P_0(t) \quad (S40c)$$

$$|3\rangle: \frac{d}{dt}P_3 = -\left(W_b^S + W_b^T + W_{3\rightarrow4}\right)P_3(t) + W^TP_1(t) + W^SP_2(t) \quad (S40d)$$

$$|4\rangle: \frac{d}{dt}P_4 = -\left(\frac{1}{\tau}\right)P_4(t) + W_{3\rightarrow4}P_3(t) + W^TP_1(t) \quad (S40e)$$

Under Tb^{III} intra-4f excitation (481 nm)

$$|0\rangle: \frac{d}{dt}P_0 = -\phi P_0(t) + \frac{1}{\tau_{Tb}}P_1(t) + \frac{1}{\tau_{Eu}}P_3(t) \quad (S41a)$$

$$|1\rangle: \frac{d}{dt}P_1 = -\left(\frac{1}{\tau_{Tb}} + W_{1\rightarrow2} + W_{1\rightarrow3}\right)P_1(t) + \phi P_0(t) \quad (S41b)$$

$$|2\rangle: \frac{d}{dt}P_2 = -W_{2\rightarrow3}P_2(t) + W_{1\rightarrow2}P_1(t) \quad (S41c)$$

$$|3\rangle: \frac{d}{dt}P_3 = -\left(\frac{1}{\tau_{Eu}}\right)P_3(t) + W_{1\rightarrow3}P_1(t) + W_{2\rightarrow3}P_2(t) \quad (S41d)$$

In Eq. S40(a-e), various states such as the ground state (S_0 at $t = 0$, transitioning to 7F_J at $t \neq 0$), T_1 , and S_1 were defined as $|0\rangle$, $|1\rangle$ and $|2\rangle$, respectively. $|3\rangle$ represents any Eu^{III} manifold other than 5D_0 , while $|4\rangle$ is the 5D_0 level. The decay lifetime values of S_1 , T_1 , and 5D_0 state, assigned as τ_S , τ_T , and τ , respectively, assume values in the range of 1 ns – 1 μs for τ_S , 1 μs – 1 ms for τ_T , and 1 ms for

⁴⁵. The intersystem crossing (ISC) rates denoted as W_{ISC} were estimated to be around 10^8 s^{-1} , considering energy gaps between S_1 and T_1 within 10000 to 15000 cm^{-1} ,⁴⁶ consistent with the system under study.

It is worth noting that considering only the Ln^{III} -to- Ln^{III} energy transfer, a few adaptations were made based on the experimental investigations. For example, no evidence of Eu^{III} - Tb^{III} energy transfer was observed. Therefore, we neglected the process of backward energy transfer when exciting the Tb^{III} , since it would account for $P_{1,2,3}$ in the coupled ODEs. Also, the 5D_1 thermal population from 5D_0 was also neglected, due to the large energy gap between the levels and rapid multiphonon deactivation of ${}^5D_1 \rightarrow {}^5D_0$ and ${}^5D_0 \rightarrow {}^7F_4$.

The population dynamics for both cases are heavily reliant on the chosen boundary conditions, ensuring that the total population across all energy levels remains constant at any given time t within the employed interval⁴⁷.

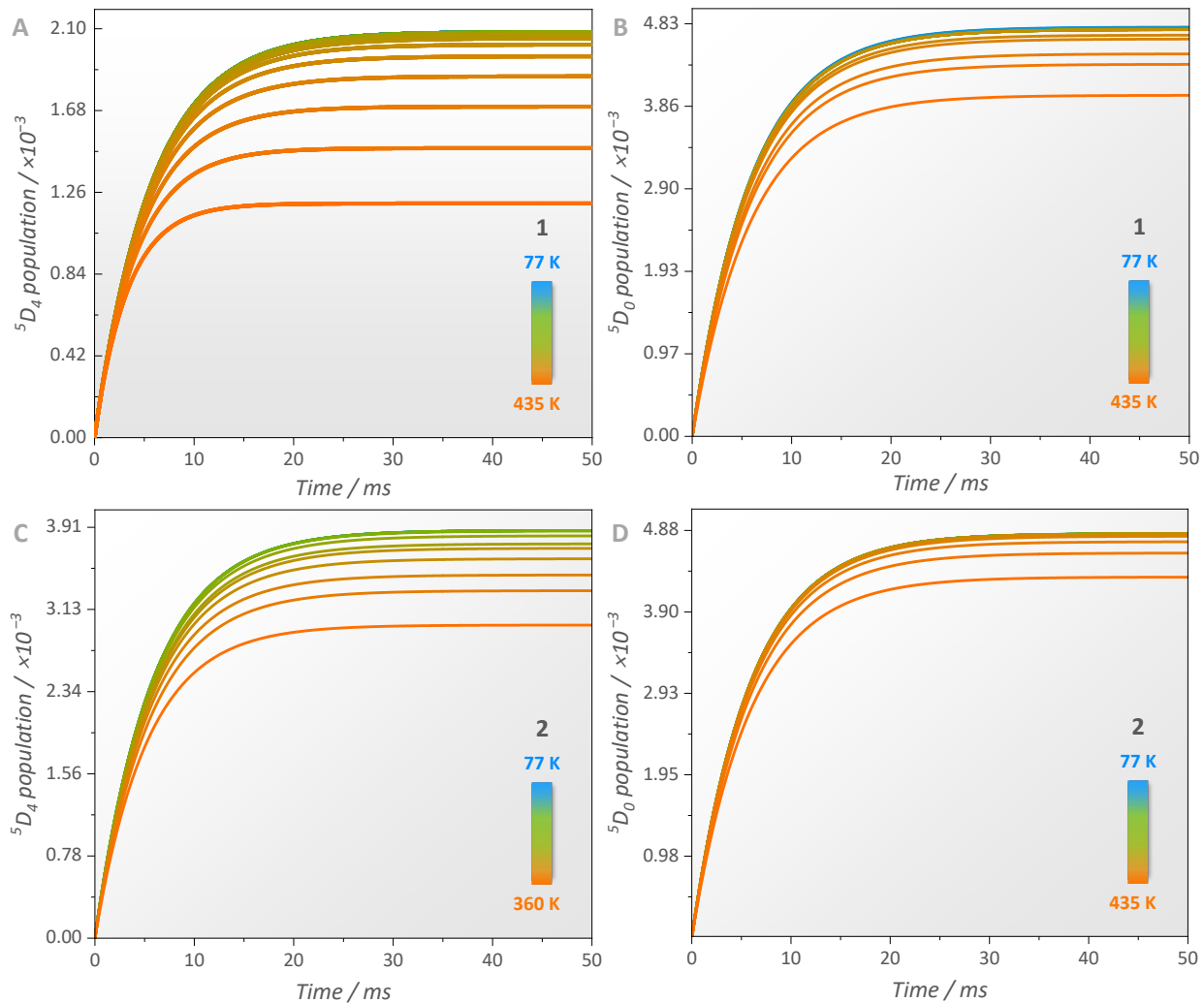


Fig S23. Population dynamics of (a) $\text{Tb}^{\text{III}}\ ^5\text{D}_4$ and (b) $\text{Eu}^{\text{III}}\ ^5\text{D}_0$ manifolds for **1**; (c) $\text{Tb}^{\text{III}}\ ^5\text{D}_4$ and (d) $\text{Eu}^{\text{III}}\ ^5\text{D}_0$ states for **2**. All calculations were performed considering the ligand's excitation (340 nm). **1** = $[\text{Ln}(\text{tfa})_3(\mu\text{-dppeo})]_n$; **2** = $[\text{Ln}(\text{tfa})_3(\mu\text{-dppbo})]_n$ ($\text{Ln} = \text{Eu}, \text{Tb}$).

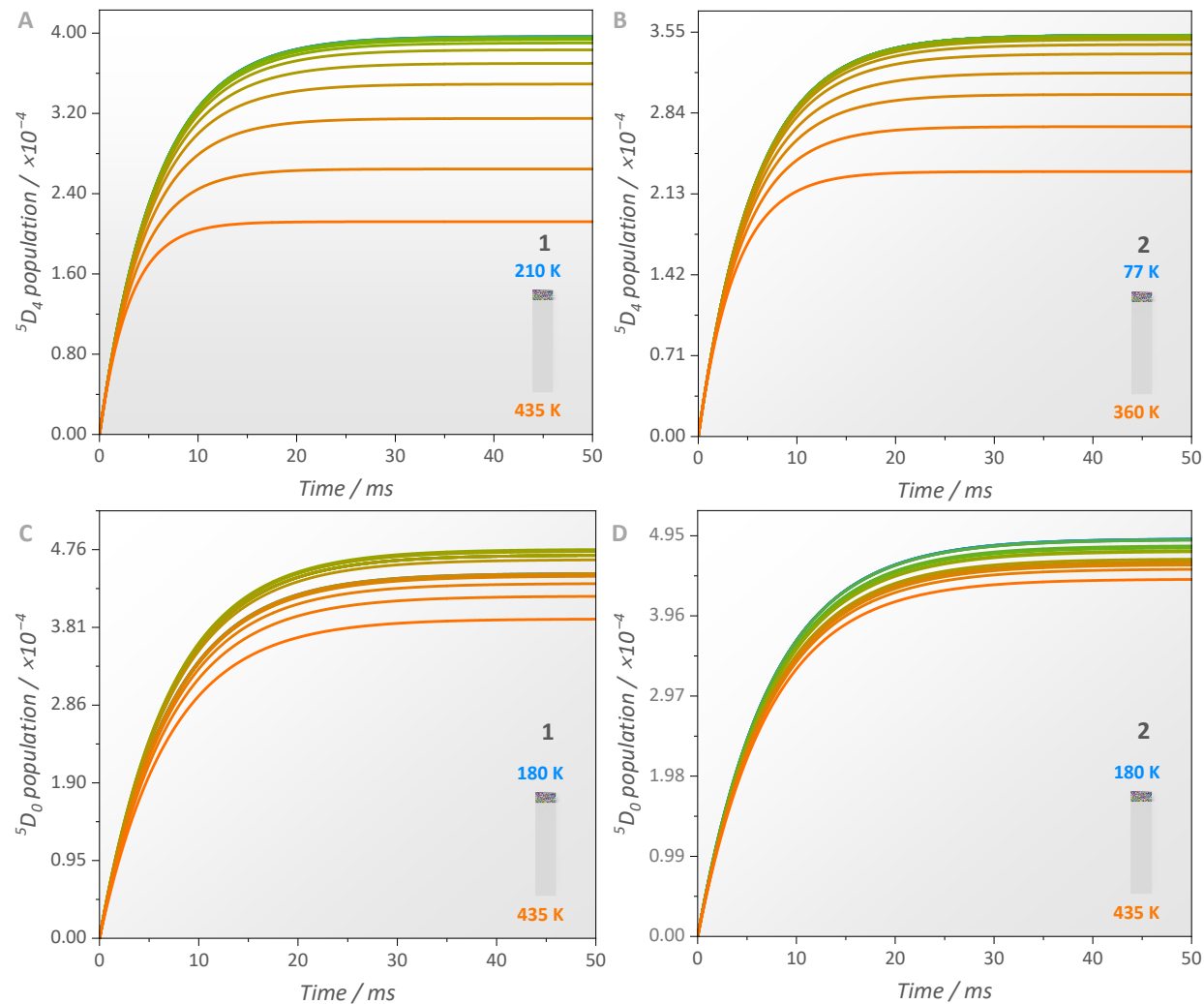


Fig S24. Population dynamics of (a) $\text{Tb}^{\text{III}}\ ^5\text{D}_4$ and (b) $\text{Eu}^{\text{III}}\ ^5\text{D}_0$ manifolds for **1**; (c) $\text{Tb}^{\text{III}}\ ^5\text{D}_4$ and (d) $\text{Eu}^{\text{III}}\ ^5\text{D}_0$ states for **2**. All calculations were performed considering the direct 4f Tb^{III} excitation (484 nm). **1** = $[\text{Ln}(\text{tfa})_3(\mu\text{-dppeo})]_n$; **2** = $[\text{Ln}(\text{tfa})_3(\mu\text{-dppbo})]_n$ ($\text{Ln} = \text{Eu}, \text{Tb}$).

Table S14. Normalized experimental and theoretical parameters for **1** and **2** under ligand excitation (340 nm). **1** = [Ln(tfa)₃(μ-dppeo)]_n; **2** = [Ln(tfa)₃(μ-dppbo)]_n (Ln = Eu, Tb).

Temperature / K	Δ _{exp(1)}	Δ _{theo(1)}	Δ _{exp(2)}	Δ _{theo(2)}
77	1	1	1	1
90	0.9679	0.9634	0.9652	0.9752
105	0.9465	0.9447	0.9505	0.9586
120	0.9246	0.9277	0.9368	0.9437
135	0.9061	0.9116	0.9254	0.9272
150	0.8929	0.8828	0.9163	0.9093
165	0.8772	0.8689	0.9092	0.8949
180	0.8617	0.8555	0.8893	0.8784
195	0.8439	0.8310	0.8459	0.8391
210	0.8294	0.8085	0.7467	0.7528
225	0.8053	0.7823	0.5908	0.6107
240	0.7731	0.7670	0.4244	0.4688
255	0.7384	0.7380	0.2865	0.3277
270	0.6981	0.6853	0.1785	0.2443
285	0.6589	0.6360	0.1025	0.1405
300	0.6041	0.5984	0.0543	0.0973
315	0.5157	0.4182	0.0269	0.0629
330	0.3930	0.2933	0.0119	0.0382
345	0.2638	0.1938	0.0044	0.0314
360	0.1554	0.0951	0.0010	0.0235
375	0.0867	0.0577	0.0006	0.0184
390	0.0422	0.0089	4.4151×10 ⁻⁴	0.0115
405	0.0175	0.0039	0.0029	0.0058
420	0.0074	0.0021	0.0067	0.0041
435	0.0048	0.0014	0.0129	0.0032

Table S15. Normalized experimental and theoretical parameters for **1** and **2** under Tb^{III} excitation (484 nm). **1** = [Ln(tfa)₃(μ-dppeo)]_n; **2** = [Ln(tfa)₃(μ-dppbo)]_n (Ln = Eu, Tb).

Temperature / K	Δ _{exp} (1)	Δ _{theo} (1)	Δ _{exp} (2)	Δ _{theo} 2
77	1	1	1	1
90	0.9604	0.9932	0.9629	0.9664
105	0.9742	0.9671	0.9422	0.9314
120	0.9229	0.9411	0.9243	0.9028
135	0.9056	0.9134	0.8945	0.8808
150	0.8454	0.8554	0.8555	0.8537
165	0.8005	0.8077	0.7974	0.8108
180	0.7496	0.7538	0.7026	0.7138
195	0.6864	0.6957	0.5444	0.5540
210	0.6183	0.6378	0.3502	0.3695
225	0.5482	0.5695	0.1981	0.2519
240	0.4786	0.4954	0.1121	0.1483
255	0.4092	0.4332	0.0661	0.0799
270	0.3408	0.3742	0.0385	0.0498
285	0.2836	0.3197	0.0210	0.0256
300	0.2260	0.2671	0.0111	0.0097
315	0.1713	0.2061	0.0056	0.0056
330	0.1159	0.1617	0.0028	0.0039
345	0.0689	0.1179	0.0014	0.0011
360	0.0371	0.0676	5.872×10 ⁻⁴	8.948×10 ⁻⁴
375	0.0180	0.0044	2.283×10 ⁻⁴	7.675×10 ⁻⁴
390	0.0082	0.0260	4.228×10 ⁻⁵	6.035×10 ⁻⁴
405	0.0034	0.0143	3.876×10 ⁻⁵	3.698×10 ⁻⁴
420	0.0016	0.0066	3.106×10 ⁻⁵	1.125×10 ⁻⁴
435	0.0025	0.0190	2.377×10 ⁻⁵	6.082×10 ⁻⁵

Supplementary note S10 – Tutorial to calculate the matrix elements

The doubly reduced matrix elements ($\langle \psi_x J_x | |\mathcal{L} + g_s \mathcal{S}| | \psi_x J_x \rangle$) of the angular \mathcal{L} and spin \mathcal{S} operators determined in Tables S1 – S3 were previously calculated in reference [24,47]. However, their calculation procedure was recently reviewed with corrections pointed out by Carneiro Neto *et al*²⁵. Since they are present in the expressions for the energy transfer rates (Eq S13 and S25), their correct determination is pivotal. Considering the selection rules, the non-null contributions are regarding transitions that obey $\Delta J = J - J' = 0, \pm 1$ (with $J = J' \neq 0$). With this in mind, the aforementioned matrix elements can be separated into two contributions (Eq S42).

$$\langle \psi' J' | |\mathcal{L} + g_s \mathcal{S}| | \psi J \rangle = \langle \psi' J' | |\mathcal{L}| | \psi J \rangle + g_s \langle \psi' J' | |\mathcal{S}| | \psi J \rangle = \sum_{i,L,S} a_i \langle \psi' J' | |\mathcal{L}| | \psi J \rangle + g_s \sum_{i,L,S} b_i \langle \psi' J' | |\mathcal{S}| | \psi J \rangle \quad (S42)$$

In these expressions, g_s is the electron *g*-factor, with value of 2.0023. Therefore, calculating the doubly reduced matrix elements reduces to obtaining the states' matrix elements considering the angular and spin operators. This can be accomplished by using the Ofelt's intermediate coupling wavefunctions²¹, obtaining the product into the same LS term, and applying Eq. S43 – S44. In these equations, J is the total angular momentum, composed by the total orbital angular momentum (L) and total spin angular momentum (S). The term in brackets {} stands for the Wigner 6-*j* symbol.

$$\langle LSJ | |\mathcal{L}| | LSJ' \rangle = (-1)^{L+S+J+1} [(2J+1)(2J'+1)(L+1)L(2L+1)]^{1/2} \begin{Bmatrix} J & 1 & J' \\ L & S & L \end{Bmatrix} \quad (S43)$$

$$\langle LSJ' | |\mathcal{S}| | LSJ \rangle = (-1)^{L+S+J'+1} [(2J+1)(2J'+1)(S+1)S(2S+1)]^{1/2} \begin{Bmatrix} S & J & L \\ J' & S & 1 \end{Bmatrix} \quad (S44)$$

It is possible to evaluate Eq S42 and obtain the values of the matrix elements.

Supplementary note S11 – Input data for the computational part

MWB52 ECP for Eu^{III} in Orca software

NewGTO Eu

S 5

1	70059.42000	0.000097
2	10776.23500	0.000707
3	2482.49010	0.003362
4	702.15260	0.010206
5	216.79260	0.016597

S 1

1	41.49500	1.0
---	----------	-----

S 1

1	29.49690	1.0
---	----------	-----

S 1

1	15.03090	1.0
---	----------	-----

S 1

1	3.77720	1.0
---	---------	-----

S 1

1	1.92190	1.0
---	---------	-----

S 1

1	0.71310	1.0
---	---------	-----

S 1

1	0.30970	1.0
---	---------	-----

S 1

1	0.05490	1.0
---	---------	-----

S 1

1	0.02270	1.0
---	---------	-----

P 6

1	4058.02070	0.000048
2	1023.32590	0.000357
3	339.38520	0.001687
4	122.34850	0.005693
5	29.05580	0.072398
6	20.62690	-0.046807

```

P 1
1    14.61790      1.0
P 1
1    5.44440      1.0
P 1
1    2.74140      1.0
P 1
1    1.22830      1.0
P 1
1    0.57690      1.0
P 1
1    0.24890      1.0
P 1
1    0.08000      1.0
D 6
1    389.08410     0.000534
2    117.76020     0.004258
3    44.98690      0.017160
4    22.85990      0.012427
5    7.83310       0.270416
6    4.11340       0.445272
D 1
1    2.09990      1.0
D 1
1    1.00430      1.0
D 1
1    0.34220      1.0
D 1
1    0.10510      1.0
F 5
1    128.23410     0.003424
2    46.26850      0.034313
3    20.73660      0.123194
4    9.44790       0.251824

```

```

5    4.31490      0.351292
F 1
1    1.91210      1.0
F 1
1    0.78970      1.0
F 1
1    0.28590      1.0
G 4
1    20.73660     0.026516
2    9.44790      0.099066
3    4.31490      0.213378
4    1.91210      0.453713
G 1
1    0.78970      1.0
G 1
1    0.28590      1.0
end

NewECP Eu

N_core 52
lmax g
s 2
1    4.742100   125.972804 2
2    2.371100   -5.265472 2
p 2
1    4.059200   86.395920 2
2    2.029600   -1.042461 2
d 2
1    2.840700   40.156495 2
2    1.420400   -0.099115 2
f 1
1    5.883800   -68.468426 2
g 1
1    1.000000   0.000000 2
end

```

MWB54 ECP for Tb^{III} in Orca software

NewGTO Tb

S 5

1	70059.42000	0.000097
2	10776.23500	0.000707
3	2482.49010	0.003362
4	702.15260	0.010206
5	216.79260	0.016597

S 1

1	41.49500	1.0
---	----------	-----

S 1

1	29.49690	1.0
---	----------	-----

S 1

1	15.03090	1.0
---	----------	-----

S 1

1	3.77720	1.0
---	---------	-----

S 1

1	1.92190	1.0
---	---------	-----

S 1

1	0.71310	1.0
---	---------	-----

S 1

1	0.30970	1.0
---	---------	-----

S 1

1	0.05490	1.0
---	---------	-----

S 1

1	0.02270	1.0
---	---------	-----

P 6

1	4058.02070	0.000048
2	1023.32590	0.000357
3	339.38520	0.001687
4	122.34850	0.005693
5	29.05580	0.072398
6	20.62690	-0.046807

P 1

1	14.61790	1.0
P	1	
1	5.44440	1.0
P	1	
1	2.74140	1.0
P	1	
1	1.22830	1.0
P	1	
1	0.57690	1.0
P	1	
1	0.24890	1.0
P	1	
1	0.08000	1.0
D	6	
1	389.08410	0.000534
2	117.76020	0.004258
3	44.98690	0.017160
4	22.85990	0.012427
5	7.83310	0.270416
6	4.11340	0.445272
D	1	
1	2.09990	1.0
D	1	
1	1.00430	1.0
D	1	
1	0.34220	1.0
D	1	
1	0.10510	1.0
F	5	
1	128.23410	0.003424
2	46.26850	0.034313
3	20.73660	0.123194
4	9.44790	0.251824
5	4.31490	0.351292

```

F 1
1    1.91210      1.0
F 1
1    0.78970      1.0
F 1
1    0.28590      1.0
G 4
1    20.73660     0.026516
2    9.44790      0.099066
3    4.31490      0.213378
4    1.91210      0.453713
G 1
1    0.78970      1.0
G 1
1    0.28590      1.0
end

NewECP Tb

N_core 54

lmax g

s 2
1    4.742100    125.972804 2
2    2.371100    -5.265472 2

p 2
1    4.059200    86.395920 2
2    2.029600    -1.042461 2

d 2
1    2.840700    40.156495 2
2    1.420400    -0.099115 2

f 1
1    5.883800    -68.468426 2

g 1
1    1.000000    0.000000 2
end
end

```

Supplementary note S12 – Python script for the population rates

Considering the ligand-to-Ln^{III} energy transfer:

```
# Population extractor
# Created by Leonardo F. Saraiva

from scipy.integrate import solve_ivp
import numpy as np

# define the rate equations. Here it is defined the populations P0, P1, P2, P3,
P4

# Considering Ligand-to-Ln ET.

# AT = 1/t(triplet); WT = foward energy transfer rate from the triplet;

# WI = intersystem crossing rate;

# AS = 1/t(singlet); WS = foward energy transfer rate from the singlet;

# phi = pump, defined as: (sigma*power*lambda) / h * c
# (cross-section * power density * exc wavelength) / planck constant * speed of
light

# W34 = multiphonon relaxation rates from the upper levels to the 5D0

# A = 1/t, where t is the lifetime of the emitting level

def f(t, y, w):
    p0, p1, p2, p3, p4 = y

    AT, WT, WI, WTb, AS, WS, WSb, phi, W34, A = w

    dp0dt = -phi*p0 + AT*p1 + AS*p2 + A*p4

    dp1dt = -(AT + WT)*p1 + WI*p2 + WTb*p3

    dp2dt = -(AS + WS + WI)*p2 + WSb*p3 + phi*p0

    dp3dt = -(WSb + WTb + W34)*p3 + WS*p2

    dp4dt = -A*p4 + W34*p3 + WT*p1
```

```

    return [dp0dt, dp1dt, dp2dt, dp3dt, dp4dt]

# Set the initial conditions and time range

# At t = 0, only the ground level is populated (p0 = 1).

y0 = [1.0, 0.0, 0.0, 0.0, 0.0]

#define the time range (0, tf). For Eu(III) complexes, usually 10 ms is
sufficient.

# Substitute the tf value in the t_eval=[] (try block).

t_span = (0, 50e-3)

# Set the values of wij (scaled down)

# w = [(1/t(triplet)), WT, WI, WTb, (1/t(singlet)), WS, WSB, phi, W34, (1/t(Eu))]

# Remove the # signal from the prior line

try:
    # Solve the system of equations numerically using Radau method
    sol = solve_ivp(f, t_span, y0, method='Radau', t_eval=np.linspace(0, 50e-3,
2000), args=(w,))

    if sol.success:
        # Extract the x and y values
        x = sol.t
        y = sol.y.T # Transpose y to match the dimensions

        # Save the values to a file
        np.savetxt('popEu105.csv', np.column_stack((x, y)), delimiter=',',
header='x,p0,p1,p2,p3,p4', comments='')

        # Alternatively, you can save them as separate arrays
        # x = sol.t
        # p0 = sol.y[0]
        # p1 = sol.y[1]
        # p2 = sol.y[2]
        # p3 = sol.y[3]
        # p4 = sol.y[4]

        # Plot the results if desired
        # import matplotlib.pyplot as plt

```

```

# plt.plot(x, p0, label='p0')
# plt.plot(x, p1, label='p1')
# plt.plot(x, p2, label='p2')
# plt.plot(x, p3, label='p3')
# plt.plot(x, p4, label='p4')
# plt.xlabel('Time')
# plt.ylabel('Values')
# plt.title('System of Equations')
# plt.legend()
# plt.show()
else:
    print('Integration failed.')
except Exception as e:
    print('Error during integration:', str(e))

```

Considering the Ln^{111} -to- Ln^{111} ET:

```

# Population extractor
# Created by Leonardo F. Saraiva

from scipy.integrate import solve_ivp
import numpy as np

# define the rate equations. Here it is defined the populations P0, P1, P2, P3.

# Considering Ln-to-Ln ET.

# phi = pumping rate.

# Atb = 1/tTb (inverse of Tb lifetime)

# AEu = 1/Eu (inverse of Eu lifetime)

# W12 = Rates of ET from 5D4 to 5D1 states, where J := 0;

# W13 = Rates of ET from 5D4 to 5D0 state;

# W23 = Rates of multiphonon decay.

def f(t, y, w):
    P0, P1, P2, P3 = y

    phi, Atb, Aeu, W12, W13, W23 = w

    dp0dt = -phi*P0 + Atb*P1 + Aeu*P3

```

```

dp1dt = -(Atb + W12 + W13)*P1 + phi*P0

dp2dt = -W23*P2 + W12*P1

dp3dt = -Aeu*P3 + W13*P1 + W23*P2

return [dp0dt, dp1dt, dp2dt, dp3dt]

# Set the initial conditions and time range

# At t = 0, only the ground level is populated (p0 = 1).

y0 = [1.0, 0.0, 0.0, 0.0]

#define the time range (0, tf). Usually 10 - 50 ms.

# Substitute the tf value in the t_eval=[] (try block).

t_span = (0, 50e-3)

# Set the values of wij (scaled down)

# w = [phi, (1/tB), (1/tEu), W12, W13, W23]

# Remove # from the previous line.

try:
    # Solve the system of equations numerically using Radau method
    sol = solve_ivp(f, t_span, y0, method='Radau', t_eval=np.linspace(0, 50e-3,
2000), args=(w,))

    if sol.success:
        # Extract the x and y values
        x = sol.t
        y = sol.y.T # Transpose y to match the dimensions

        # Save the values to a file
        np.savetxt('pop.csv', np.column_stack((x, y)), delimiter=',',
header='x,P0,P1,P2,P3', comments='')

        # Alternatively, you can save them as separate arrays
        # x = sol.t
        # p0 = sol.y[0]
        # p1 = sol.y[1]

```

```
# p2 = sol.y[2]
# p3 = sol.y[3]

# Plot the results if desired
# import matplotlib.pyplot as plt
# plt.plot(x, p0, label='p0')
# plt.plot(x, p1, label='p1')
# plt.plot(x, p2, label='p2')
# plt.plot(x, p3, label='p3')
# plt.plot(x, p4, label='p4')
# plt.xlabel('Time')
# plt.ylabel('Values')
# plt.title('System of Equations')
# plt.legend()
# plt.show()

else:
    print('Integration failed.')
except Exception as e:
    print('Error during integration:', str(e))
```

References

- ¹ D. A. Lima, A. G. Bispo-Jr, D. A. Galico, S. F. N. Coelho, J. H. Araújo Neto, J. A. Ellena, L. Petiote, I. O. Mazali, F. A. Sigoli, *Inorg. Chem.* **2023**, 62, 6808–6816.
- ² C. D. S. Brites, A. Millán, L. D. Carlos, Chapter 281 - Lanthanides in Luminescent Thermometry. In: *Handbook on the Physics and Chemistry of Rare Earths*; Bunzli, J-C.; Pecharsky, V. Eds.; Elsevier: Amsterdam, **2016**; Vol. 49, 339–427.
- ³ F. Neese, *WIREs Comput. Mol. Sci.* **2022**, 12:e1606.
- ⁴ C. Adamo, M. Cossi, V. Barone, *J. Mol. Struc. Theochem.* **1999**, 493, 145 – 157.
- ⁵ E. Caldeweyher, J-M. Mewes, S. Ehlert, S. Grimme, *Phys. Chem. Chem. Phys.* **2020**, 22, 8499 – 8512.
- ⁶ F. Weigend, R. Ahlrichs, *Phys. Chem. Chem. Phys.* **2005**, 7, 3297 – 3305.
- ⁷ J. Yang, S. Falleta, A. Pasquarello, *npj Comput. Mat.* **2023**, 9, 108.
- ⁸ M. Dolg, H. Stoll, A. Savin, H. *Theor. Chim. Acta* **1989**, 75, 173 – 194.
- ⁹ M. Dolg, H. Stoll, A. Savin, H. Preuss, *Theor. Chim. Acta* **1993**, 85, 441 – 450.
- ¹⁰ R. T. Moura Jr, A. N. Carneiro Neto, E. C. Aguiar, C. V. Santos-Jr, E. M. de Lima, W. M. Faustino, E. E. S. Teotonio, H. F. Brito, M. C. F. C. Felinto, R. A. S. Ferreira, R. A. S.; L. D. Carlos, R. L. Longo, O. L. Malta, *Opt. Mat. X* **2021**, 11, 100080.
- ¹¹ C. V. Santos-Jr, E. C. Aguiar, A. N. Carneiro Neto, A. R. T. Moura Jr, *Opt. Mat. X* **2023**, 20, 100275.
- ¹² O. L. Malta, E. A. Gouveia, *Phys. Lett. A* **1983**, 97, 333 – 334.
- ¹³ R. T. Moura Jr, M. Quintano, C. V. Santos-Jr, V. A. C. A. Albuquerque, E. C. Aguiar, E. Kraka, A. N. Carneiro Neto, *Opt. Mat. X* **2022**, 16, 100216.
- ¹⁴ O. L. Malta, *Chem. Phys. Lett.* **1982**, 87, 27 – 29.
- ¹⁵ Carlos, L. D.; Malta, O. L.; Albuquerque, R. Q. A covalence fraction model for lanthanide compounds, *Chem. Phys. Lett.* **2005**, 415, 238 – 242.
- ¹⁶ A. N. C. Neto, E. E. S. Teotonio, G. F. de Sá, H. F. Brito, J. Legendziewicz, L. D. Carlos, M. C. F. C. Felinto, P. Gawryszewska, R. T. Moura Jr, R. L. Longo, W. M. Faustino, O. L. Malta, In: *Handbook on the Physics and Chemistry of Rare Earths*, **2019**, 56, 55.
- ¹⁷ O. L. Malta, **1997**, 71, 3, 229 – 236
- ¹⁸ O. L. Malta, F. R. Gonçalves e Silva, *Spectroch. Acta Part A Mol. Biomol. Spec.* **1998**, 54, 11, 1593 – 1599.
- ¹⁹ O. L. Malta, *J. Non-Cryst. Sol.* **2008**, 354, 42 – 44, 4770 – 4776.
- ²⁰ W. T. Carnall, P. R. Fields, K. Rajnak, *J. Chem. Phys.* **1968**, 49, 4450 – 4455.
- ²¹ G. S. Ofelt, *J. Chem. Phys.* **1963**, 38, 2171 – 2180.
- ²² E. Kasprzycka, A. N. Carneiro Neto, V. A. Trush, L. Jerzykiewicz, V. M. Amirkhanov, O. L. Malta, J. Legendziewicz, P. Gawryszewska, *J. Rare Earths*, **2020**, 38, 552.
- ²³ Judd, B. R. *Operator Techniques in Atomic Spectroscopy*, McGraw-Hill Book Company: New York, 1998.
- ²⁴ A. N. Carneiro Neto, R. T. Moura Jr, A. Schyichuk, V. Paterlini, F. Piccinelli, M. Bettinelli, O. L. Malta, *J. Phys. Chem. C* **2020**, 124, 18, 10105 – 10116.
- ²⁵ A. N. Carneiro Neto, R. T. Moura Jr, J. A. A. Coelho, M. E. Silva-Jr., J. L. Costa, O. L. Malta, R. L. Longo, *Chinese J. Lumin.* **2022**, 43, 12, 1871 – 1891.
- ²⁶ W. T. Carnall, P. R. Fields, K. Rajnak, *J. Chem. Phys.* **1968**, 49, 4424 – 4442.
- ²⁷ S. Edvardsson, M. Klintenberg, *J. Alloys Comp.* **1998**, 275 – 277, 230 – 233.
- ²⁸ B. G. Wybourne, *J. Chem. Phys.* **1962**, 36, 2301 – 2311.
- ²⁹ K. Rajnak, *J. Chem. Phys.* **1965**, 43, 847 – 855.
- ³⁰ L. A. Riseberg, L. A.; H. W. Moos, *Phys. Rev.* **1968**, 174, 429.
- ³¹ H. W. Moos, *J. Lumin.* **1970**, 1 – 2, 106 – 121.
- ³² L. A. Riseberg, M. J. Weber, *Progress in Opt.* **1977**, 14, 89 – 159.
- ³³ L. A. Riseberg, W. B. Gandrud, H. W. Moos, *Phys. Rev.* **1967**, 159, 262 – 266.
- ³⁴ T. Miyakawa, D. L. Dexter, *Phys. Rev. B* **1970**, 1, 27 – 29.
- ³⁵ A. De, M. A. Hernandez-Rodriguez, A. N. Carneiro Neto, V. Dwij, V. Sathe, L. D. Carlos, R. Ranjan, *J. Mat. Chem. C* **2023**, 11, 6095 – 6106.

-
- ³⁶ E. Hairer, G. Wanner, *J. Comp. Appl. Math.* **1999**, 111, 93 – 111.
- ³⁷ A. N. Carneiro Neto, E. Mamontova, A. M. P. Botas, C. D. S. Brites, R. A. S. Ferreira, J. Rouquette, Y. Guari, J. Larionova, J. Long, L. D. Carlos, *Adv. Opt. Mat.* **2022**, 10, 2101870.
- ³⁸ M. Fang, A. N. Carneiro Neto, L. Fu, R. A. S. Ferreira, V. deZeaBermudez, L. D. Carlos, *Adv. Mat. Tech.* **2022**, 7, 2100727.
- ³⁹ L. Fu, Y. Wu, T. Fu, *J. Lumin.* **2022**, 245, 118758.
- ⁴⁰ W. T. Carnall, H. Crosswhite, M. H. Crosswhite, Energy Level Structure and Transition Probabilities in the Spectra of the Trivalent Lanthanides in LaF₃, Argonne, IL, United States, 1978.
- ⁴¹ E. Kasprzycka, A. N. Carneiro Neto, V. A. Trush, O. L. Malta, L. Jerzykiewicz, V. M. Amirkhanov, J. Legendziewicz, P. Gawryszewska, *Spectrochimica Acta Part A Mol. Biomol. Spec.* **2022**, 274, 121072.
- ⁴² Cameron F. Holder, Raymond E. Schaak, *ACS Nano* **2019**, 13, 7359–7365.
- ⁴³ L. Lv, K. Yuan, T. Zhao, Y. Wang, *J. Mat. Chem. C*, **2020**, 8, 10369 – 10381.
- ⁴⁴ F. Di Maiolo, D. K. A. Phan Huu, D. Giavazzi, A. Landi, O. Racchi, A. Painelli, *Chem. Sci.* **2024**, 15, 5434 – 5450.
- ⁴⁵ J. F. C. B. Ramalho, A. N. Carneiro Neto, L. D. Carlos, P. S. André, R. A. S. Ferreira, Chapter 324 - Lanthanides for the new Generation of optical sensing and internet of things. In: *Handbook on the Physics and Chemistry of Rare Earths*; Bunzli, J-C.; Pecharsky, V. K. Eds.; Elsevier: Amsterdam, **2022**, vol. 61. 31 – 128.
- ⁴⁶ I. M. S. Diogenis, A. G. Bispo-Jr, R. V. Pirovani, L. F. Saraiva, F. C. Gozzo, C.R.D Correia, I. O. Mazali, R. A. Nome, F. A. Sigoli, *J. Mat. Chem. C*, **2024**, 12, 5097 – 5107.
- ⁴⁷ L. Blois, L.; A. N. Carneiro Neto, O. L. Malta, H. F. Brito, *J. Lumin.* **2022**, 274, 118862.